Strongly-Coupled Conjugate Heat Transfer Investigation of Internal Cooling of Turbine Blades using the Immersed Boundary Method

Tae Kyung Oh

Thesis submitted to the faculty of the Virginia Polytechnic Institute and State University in partial fulfillment of the requirements for the degree of

Master of Science
In
Mechanical Engineering

Danesh K. Tafti – Chair
Roop L. Mahajan
Wing F. Ng

May 13th 2019
Blacksburg, Virginia, USA

Keywords: Conjugate heat transfer, immersed boundary method, internal cooling, fully developed assumption

Strongly-Coupled Conjugate Heat Transfer Investigation of Internal Cooling of Turbine Blades using the Immersed Boundary Method

Tae Kyung Oh

ABSTRACT

The present thesis focuses on evaluating a conjugate heat transfer (CHT) simulation in a ribbed cooling passage with a fully developed flow assumption using LES with the immersed boundary method (IBM-LES-CHT). The IBM with the LES model (IBM-LES) and the IBM with CHT boundary condition (IBM-CHT) frameworks are validated prior to the main simulations by simulating purely convective heat transfer (iso-flux) in the ribbed duct, and a developing laminar boundary layer flow over a two dimensional flat plate with heat conduction, respectively.

For the main conjugate simulations, a ribbed duct geometry with a blockage ratio of 0.3 is simulated at a bulk Reynolds number of 10,000 with a conjugate boundary condition applied to the rib surface. The nominal Biot number is kept at 1, which is similar to the comparative experiment. As a means to overcome a large time scale disparity between the fluid and the solid regions, the use of a high artificial solid thermal diffusivity is compared to the physical diffusivity. It is shown that while the diffusivity impacts the instantaneous fluctuations in temperature, heat transfer and Nusselt numbers, it has an insignificantly small effect on the mean Nusselt number. The comparison between the IBM-LES-CHT and iso-flux simulations shows that the iso-flux case predicts higher local Nusselt numbers at the back face of the rib. Furthermore, the local Nusselt number augmentation ratio (EF) predicted by IBM-LES-CHT is compared to the body fitted grid (BFG) simulation,

experiment and another LES conjugate simulation. Even though there is a mismatch between IBM-LES-CHT prediction and other studies at the front face of the rib, the area-averaged EF compares reasonably well in other regions between IBM-LES-CHT prediction and the comparative studies.

Strongly-Coupled Conjugate Heat Transfer Investigation of Internal Cooling of Turbine Blades using the Immersed Boundary Method

Tae Kyung Oh

General Audience Abstract

The present thesis focuses on the computational study of the conjugate heat transfer (CHT) investigation on the turbine internal ribbed cooling channel. Plenty of prior research on turbine internal cooling channel have been conducted by considering only the convective heat transfer at the wall, which assumes an iso-flux (constant heat flux) boundary condition at the surface. However, applying an iso-flux condition on the surface is far from the realistic heat transfer mechanism occurring in internal cooling systems. In this work, a conjugate heat transfer analysis of the cooling channel, which considers both the conduction within the solid wall and the convection at the ribbed inner wall surface, is conducted for more realistic heat transfer coefficient prediction at the inner ribbed wall.

For the simulation, the computational mesh is generated by the immersed boundary method (IBM), which can ease the mesh generation by simply immersing the CAD geometry into the background volume grid. The IBM is combined with the conjugate boundary condition to simulate the internal ribbed cooling channel.

The conjugate simulation is compared with the experimental data and another computational study for the validation. Even though there are some discrepancy between the IBM simulation and other comparative studies, overall results are in good agreement. From the thermal prediction comparison between the iso-flux case and the conjugate case

using the IBM, it is found that the heat transfer predicted by the conjugate case is different from the iso-flux case by more than 40 percent at the rib back face.

The present study shows the potential of the IBM framework with the conjugate boundary condition for more complicated geometry, such as full turbine blade model with external and internal cooling system.

Acknowledgements

I would first like to thank my advisor, Dr. Danesh Tafti for his guidance, patience and motivation during my research. Throughout my Master study, he provided me great academic knowledge and thoughtful discussion. Furthermore, as a research advisor, he helped and encouraged me to think like a true researcher.

I would also like to thank Dr. Roop Mahajan and Dr. Wing Ng for taking their precious time to be my committee members and reviewing my research work.

I would also like to thank my colleagues – Susheel, Peter, Husam, Ze, Aevelina, Mahammad, Vicky and Vivek, who shared their knowledge with me for my research. I also thank the support provided by Advanced Research Computing at Virginia Tech.

Finally, I would like to express my profound gratitude to my parents for providing me unfailing support and continuous encouragement during my years of study. This accomplishment would not have been possible without them.

Table of Contents

List of Figures

List of Tables

Chapter 1

Introduction

1.1 Motivation and Background

In modern gas turbine applications, higher thermal efficiency and power output are essential and highly demanded. Two significant parameters of the gas turbine engine performance are compression ratio and turbine inlet temperature based on the Brayton cycle. Advanced gas turbine inlet temperatures (~1300℃-1700℃), however, already far exceed the thermal limitation of materials commonly used in the blade. Such high inlet temperatures may cause excessive thermal stress on the blade and would critically affect structural reliability [1]. In this regard, various cooling technologies are applied to turbine blades to keep the blade metal temperature within an acceptable range. Thus significant amount of research has been performed on the modern turbine cooling system to measure and improve its cooling performance. However, it is reported that the blade life span can be reduced by half with under-prediction of blade metal temperature by 30℃ [2]. Therefore, advances in thermal prediction of the turbine blade using more accurate thermal analysis is necessary to prevent thermal failure.

Figure 1.1 shows the geometry of a typical turbine blade used in modern gas turbine applications. Turbine cooling technologies are categorized into two main parts. First, the turbine blade is cooled convectively by circulating relatively cool air (~600℃) from the compressor, bypassing the combustion chamber, through internal channels in the blade (internal cooling). The air flows through the internal cooling channels that typically have turbulator (ribs, dimples, pins, protrusions) to enhance flow turbulence to augment the heat transfer on the channel inner surface so more heat can be transferred to the cooling air. Second, the internal cooling air is bled out from

inside the blade through cooling holes. This bled air forms a protective layer on the blade surface to shield the surface from a hot mainstream (film cooling) [3].

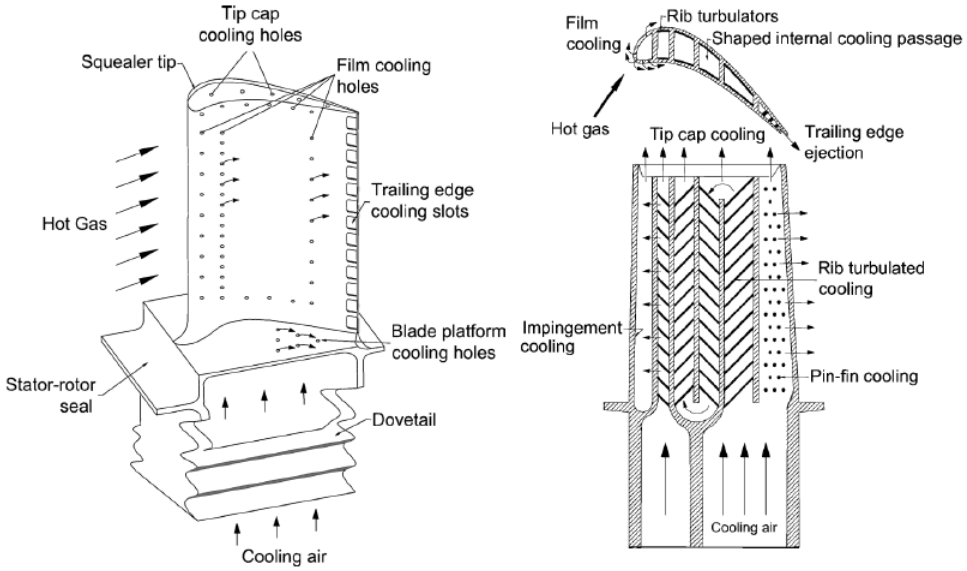

Figure 1.1: Exterior and interior geometries of turbine blade [2].

1.1.1 Conjugate Heat Transfer

Gas turbine blade cooling systems are quite complicated due to their complex design and the presence of both convection and conduction heat transfer in the blade material. Many investigations, both experimental and computational, have been performed to investigate turbulent convection heat transfer in internal cooling geometries. This is done by assuming either a constant temperature or constant heat flux (iso-flux) condition on the surface. While this condition simplifies the boundary condition to calculate the heat transfer at the solid-fluid interface, it is not representative of the actual thermal conditions. As the need to predict blade metal temperatures becomes more critical, the accurate thermal prediction of turbine cooling systems require that both convection and conduction be considered in the analysis. In this thesis, a conjugate heat transfer (CHT), which considers both heat convection to the fluid and conduction in the solid, is considered to investigate more realistic thermal phenomena in the internal cooling channel.

In CHT analysis, the Biot number (*Bi*), defined as the ratio of the resistance to solid conduction to the resistance to fluid convection across the fluid boundary layer, plays an important role. In general, Biot numbers much less than 0.1 would result in a near-uniform temperature in the solid. In such cases, the resistance to conduction in the solid is much less ($k_s \uparrow$) than the resistance to convection in the fluid ($h \downarrow$). Consequently, for extreme Biot numbers, be they tending to zero or infinity, conjugate analysis is irrelevant.

Solving conjugate heat transfer problem requires a thermal analysis in both fluid and solid regions. In general, there are two main numerical approaches to solve conjugate problems. The first approach (strong coupling approach) solves both fluid and solid regions simultaneously as a single large system of equations. The second approach (weak coupling approach) solves each region sequentially using dedicated solvers that exchange boundary conditions with each other [4]. One of the drawbacks of the second approach is that it requires sequential iterations between fluid and solid regions, which may be less efficient than the first approach in terms of computational cost [5]. In this thesis, a strong coupling approach is used for the conjugate simulation. Challenges associated with disparate solid and fluid time scales are discussed and solutions provided.

1.1.2 Immersed Boundary Method

In addition to convection-conduction coupled analysis, the intricate geometries of turbulence promoting cooling channel surfaces pose another simulation challenge. Body fitted grid (BFG) is commonly used in the computational domain for simulations; However, in the complex internal cooling geometries with ribs, pins, cooling holes, impingement cooling, etc., it is hard to construct the complex grid. With the aim of resolving the complex internal cooling geometries, the immersed boundary method (IBM) is used in this thesis. In IBM, instead of the grid conforming to the body shape, the body is placed in a background grid which is fixed. In the IBM, the desired

geometry (immersed surface) is defined by a surface mesh that is placed in a background volume mesh in which solid and fluid regions are identified. The utility of IBM to simulate dynamic surfaces in a fluid has been widely reported. In contrast to the convenience of not necessitating intricate mesh generation, IBM requires a fine grid near the immersed surface to accurately represent the boundary conditions. More detail implementation of IBM, particurly for CHT calculations, is discussed in Chapter 2.

1.2 Literature Review

1.2.1 Background Review

Plenty of prior research has been conducted to understand the mechanism of heat transfer and to improve the design of turbine cooling systems. Researchers have performed various experiments on internal cooling passages by changing the channel design parameters of ribbed ducts (channel aspect ratio: height to width ratio, the rib shape, the blockage ratio: rib height to hydraulic diameter ratio, etc.) [7 – 11] and examining alternative turbulators, such as dimples, pins and protrusions on the cooling passage. On the numerical side, different turbulence models have been used to conduct fluid flow and heat transfer simulations in internal cooling passages. In early studies, RANS $\mathrm{k}-\varepsilon$, $\mathrm{k}-\omega$ and v^2-f models [12 – 14] were used. With advances in computational power and numerical methodologies, more accurate means of computing turbulence, such as using Large Eddy Simulation (LES) [15 – 18] and hybrid RANS-LES [18] have been used recently for similar investigations.

1.2.2 Analytical Conjugate Studies Review

Luikov [19] and Payvar [20] emphasized the heat transfer dependence on the conductivity ratio and the Burn number between the solid and fluid. They derived analytical solutions in a laminar zero-pressure gradient boundary layer with conjugate heat transfer to a plate of finite-thickness.

The Brun number proposed by Luikov *et al*. is identical to the Biot number which gives the ratio of thermal resistance of solid conduction to the resistance of convection across the fluid boundary layer. From the analysis, for a Brun number of 0.1, the Nusselt number starts varying from the canonical value and this discrepancy becomes more than 50 % as the Brun number increases for a developing laminar boundary layer. Subsequent researchers [22 – 24] used alternative analytical approaches to solve the same conjugate problem, and validated their solutions by comparing them to solutions of Luikov and Payvar.

1.2.3 Experimental Studies Review

Since 1980s, many researchers have performed conjugate heat transfer (CHT) investigation on the turbine blade. Conjugate Heat Transfer (CHT) experiments using turbine blades were initiated by Hylton *et al*. [24]. and Turner *et al*. [25] for the full NASA C3X vane. Even though the experimental Biot numbers for these experiments were not reported, these have been widely used as the benchmark datasets for full blade computational studies, and provide an insight into the thermal field of the conducting vane.

For a better understanding of the thermal behavior of the conjugate condition, subsequent researchers performed investigations at various Biot numbers, including those associated with actual engine conditions. Sweeny and Rhodes [26] performed an experiment for a conjugate case at a Biot number representing the actual engine condition. The experiment was performed on a flat plate that has both external film cooling holes and an internal impingement cooling design. The result showed that closely spaced film cooling holes had a larger effect on improving overall cooling effectiveness than angled film cooling holes. Jung *et al*. [27] conducted a similar experimental investigation on film cooling with an internal impingement array at various Biot numbers (0.06 – 4.04). They showed that as the Biot number decreased from 4.04 to 0.06,

indicative of convective cooling dominating over conduction through the solid, the averaged total cooling effectiveness increased by about 23% due to the higher thermal conductivity of the solid.

Li *et al*. [28] experimentally investigated conjugate heat transfer on a pin-fin array. A liquid crystal sheet and subsequent FEM analysis were used to measure an accurate temperature field of the whole solid pin-fin array. Three different thermal conductivities are tested for the investigation and compared with a purely convective case. The results showed that all three conjugate cases exhibit 8-31% higher effective Nusselt numbers than for the purely convective case.

Several experiments involving conjugate heat transfer in internal ribbed ducts have been conducted at the von Karman Institute (VKI) [30 – 33]. For example, Cukurel and Arts [33] performed an experimental investigation of an internal cooling passage at Re = 40,000 (based on the hydraulic diameter), with a blockage ratio of 0.3. The mean heat transfer enhancement factor for this conjugate case was shown to deviate from the idealized convective case by 26%, -5% and 55% at the front, top and back faces of the rib. This investigation demonstrated that a coupled conduction-convection boundary condition at the rib surface can have a significant impact on the computed heat transfer values.

1.2.4 Numerical Conjugate Studies Review

Several researchers have used commercial CFD codes to conduct a conjugate analysis on the turbine cooling systems. Ke and Wang [33] used ANSYS CFX 14.5 with the $k-\omega$ SST model to investigate conjugate heat transfer of the entire C3X turbine vane. For the validation of the turbulence model and their numerical procedure, they compared the temperature field with the experimental results of Hylton *et al*. [25], and showed good agreement. Facchini *et al.* [34] performed a similar conjugate investigation using STAR-CD with three different turbulence models: a low Re $k-\varepsilon$ model, RNG $k-\varepsilon$ model and a high Re $k-\varepsilon$ model. The validation with

Hylton *et al* [25], however, showed that heat transfer coefficients over the entire blade were significantly overpredicted for all three turbulence models.

Dyson *et al*. [35] also used the $k-\omega$ SST model of ANSYS FLUENT to simulate the conjugate experiments of Williams et al. [36]. Dyson *et al*. over-predicted the overall cooling effectiveness for a setup that combined two film cooling holes and an internal impingement cooling design.

Shih *et al*. [37] studied the effect of the Biot number for a flat plate combined with a ribbed cooling passage using ANSYS FLUENT with k-ε model. They showed that the Biot number strongly affected the temperature of the flat plate and the internal cooling passage by simulating a range of Biot numbers (0.4-6). At low Biot numbers, which correspond to higher heat flux within the solid, the temperature within the solid region showed a more uniform distribution than at higher Biot numbers.

In-house developed CFD solvers using either strong or weak coupling approach have been used widely to study a conjugate problem. Han *et al.* [38] developed 2-D and 3-D conjugate heat transfer prediction code using a strong coupling approach. For their simulation, airfoils were constructed using a hybrid unstructured grid for both 2-D and 3-D cases. The 2-D airfoil was simulated for the transonic turbine airfoil cascade flow, and compared with the experiment by Giel *et al.* [39], [40] to validate the transonic turbulence flow field. The pressure on the blade surface in the simulation matched well with the experimental result by Giel *et al.* However, the temperature distribution near the airfoil was not directly compared with any other comparative studies. For the 3-D case validation, a hollow sphere with isothermal boundary condition was simulated and compared with the analytical solution. The computed radial temperature distribution matched well with the analytical solution. In addition, the temperature distribution near the 3-D airfoil with

conjugate boundary condition was calculated; however, direct comparison with other validated studies was not reported in the paper.

Song *et al.* [41] validated their immersed boundary method with conjugate boundary condition using three different conjugate heat transfer problems, which are channel flow with conducting walls, channel flow with a heated obstacle and a conducting cylinder array. Different solid - fluid thermal conductivity ratios were tested for all studies with the solid to fluid thermal storage ratio of 1. The authors concluded that their IBM with CHT calculation was validated by comparing their three different studies with analytical and previous numerical simulations. However, only two dimensional and laminar flow simulations were shown in this paper.

Bohn *et al.* [42] developed an in-house conjugate solver, CHTflow, using a weak coupling approach. CHTflow solves the Navier-Stokes equations in the fluid region and Fourier equation in the solid region. Following this study, Bohn and his collaborators have performed numerical conjugate analysis on various turbine cooling systems [44 – 46]. Bohn *et al.* used CHTflow to investigate conjugate heat transfer rate of film cooling holes [46]. A hot gas flow in a duct with cooling holes was set for the simulation with adiabatic and conjugate duct wall boundary condition cases. In the result, the temperature distribution in the wall region after the cooling holes was higher for the conjugate condition than the adiabatic condition due to a heat flux through the solid from the hot gas flow. More recently, CHTflow was used to investigate the leading edge of the turbine blade with 54 film cooling holes and smooth internal cooling channel configuration [47]. Along with the simulation, the experimental investigation was performed as a comparative study; however, the ribbed internal cooling channel design is used. The temperature distribution was shown to be slightly higher for the simulation than the experiment. It was concluded that the difference was due to the use of the smooth internal cooling channel for the simulation, which has

less heat transfer rate. Although there was a little difference in the surface temperature comparison, overall trends of temperature and cooling effectiveness distributions on the blade showed relatively good agreement.

Scholl *et al*. [48] used the weak coupling approach to conduct conjugate analysis on a square ribbed duct at Re = 40,000 and blockage ratio of 0.3 using an LES fluid solver (AVBP) and a solid conduction solver. In-house developed LES fluid and conduction solvers (AVTP) were used for the conjugate calculation. When compared to a purely convective test case, the overall area-averaged enhancement factor of the rib for the conjugate case was lower than the convective case by about 13%. Especially, the result of the conjugate case showed about 30% lower heat transfer on the back face of the rib than the convective case. The authors concluded that a conjugate simulation was necessary for an accurate heat transfer prediction, since the iso-flux assumption significantly over-predicts the wall temperature, particularly at the vicinity of the rib, when compared to experiment.

1.3 Thesis Objectives

Combined IBM-LES is not widely used for turbulent flows at high Reynolds numbers because of the incompatibility between a non-body-fitted background grid and the need to resolve the thin and energetic inner wall layers of turbulent boundary layers. Further, combining IBM-LES with conjugate heat transfer (IBM-LES-CHT) has not been attempted in the gas turbine literature, nor to the best of our knowledge in the broader literature. The over-arching objective is to establish the feasibility of this procedure for application to more complex geometries by critical evaluation in a canonical geometry of a ribbed duct. This thesis primarily focuses on a strongly-coupled CHT analysis of an internal cooling duct using Large-eddy Simulations (LES) under a fully developed assumption. An in-house developed solver, GenIDLEST [49] is used to calculate both fluid and

solid domains. The IBM framework is used to resolve geometrical features in the simulation. A fully-developed assumption and wall modeled LES method are used to reduce the computational complexity of the problem..

The thesis is organized as follows[1]:

- Chapter 2: Numerical methodology and governing equations are discussed. The IBM framework is described and the conjugate boundary condition treatment is discussed.
- Chapter 3: LES solver with IBM framework (IBM-LES) is validated by simulating an internal cooling channel in a fully developed duct with square ribs at $Re_b \sim 10{,}000$. The flow field and turbulence intensity results are shown and compared with simulations using a body fitted grid and with experimental data by Casarsa and Arts [6, 64, 65].
- Chapter 4: Conjugate treatment with IBM (IBM-CHT) is validated by simulating a laminar flow on a flat plate. Re_L = 24,000 and various solid to fluid conductivity ratios are simulated. The local Nusselt number and the temperature field at solid - fluid interface is compared with an analytical solutions by Payvar [21].
- Chapter 5: IBM with conjugate treatment is used for ribbed duct simulation at $Re_b \sim 10{,}000$ with fully a developed assumption (IBM-LES-CHT). Use of both accelerated (case 1) and actual (case 2) solid thermal diffusivity are discussed. The local Nusselt number distribution at the symmetry plane is compared with experimental data by Cukurel and Arts [32] and LES - Conjugate simulation with weak coupling approach by Scholl *et al*. [49].

[1] Some of the contents of this thesis have been adapted from the paper:
Oh T.K., Tafti, D. K. and Nagendra, K. "LES-Conjugate heat transfer analysis of a ribbed cooling passage using the immersed boundary method," Paper No. GT2019-90397, Proceedings of the ASME Turbo Expo 2019: Turbomachinery Technical Conference & Exposition (TURBO EXPO 2019), June 17-21, 2019, Phoenix, Arizona, USA.

Chapter 2

Numerical Methodology

In this chapter, the governing equations and numerical methods (fully developed assumption, immersed boundary method, and wall modeled LES) used in the simulations are introduced. For all simulations, the in-house developed LES solver - Generalized Incompressible Direct and Large Eddy Simulation of Turbulence (GenIDLEST) [6] is used to calculate flow and thermal fields.

2.1 Governing Equation

Following sets of parametrizations are used to non-dimensionalize the governing equations. The superscript * used in the equations below represents dimensional variables.

$$\rho = \frac{\rho^*}{\rho^*_{ref}}\,;\ \mu = \frac{\mu^*}{\mu^*_{ref}}\,;\ \vec{x} = \frac{\vec{x}^*}{L^*_{ref}}\,;\ \vec{u} = \frac{\vec{u}^*}{U^*_{ref}}\,;\ t = \frac{t^* U^*_{ref}}{L^*_{ref}};\ \theta = \frac{T^* - T^*_{ref}}{T^*_0}\,;\ P = \frac{P^* - P^*_{ref}}{\rho^*_{ref} {U^*_{ref}}^2};$$

$$k = \frac{k^*}{k^*_{ref}};\ C_p = \frac{C^*_p}{C^*_{P_{ref}}};\ Re_{ref} = \frac{\rho^*_{ref} U^*_{ref} L^*_{ref}}{\mu^*_{ref}};\ Pr_{ref} = \frac{\mu^*_{ref} C^*_{P_{ref}}}{k^*_{ref}} \tag{2.1}$$

With these parameterizations and a low Mach number assumption, the non-dimensional form of the governing equations (continuity, momentum and energy) for the incompressible flow are written as follow,

Continuity:

$$\frac{\partial \rho u_i}{\partial x_i} = 0 \tag{2.2}$$

Momentum:

$$\frac{\partial \rho u_i}{\partial t} + \frac{\partial (\rho u_j u_i)}{\partial x_j} = -\frac{\partial P}{\partial x_i} + \frac{1}{Re_{ref}} \frac{\partial}{\partial x_j}\left[(\mu + \mu_t)\frac{\partial u_i}{\partial x_j}\right] + \beta \vec{e}_x \tag{2.3}$$

Energy:

$$\frac{\partial \rho \theta}{\partial t} + \frac{\partial (\rho u_j \theta)}{\partial x_j} = \frac{1}{C_p \cdot Re_{ref} \cdot Pr_{ref}} \frac{\partial}{\partial x_j}\left[(k + k_t)\frac{\partial \theta}{\partial x_j}\right] - \rho \gamma u_x \tag{2.4}$$

The governing equations are discretized using a finite-volume procedure. A second-order central difference scheme is used for both the convection as well as the viscous terms. A fractional-step algorithm is used to advance the equations in time by calculating an intermediate velocity field in the first step and then correcting the velocity field to satisfy discrete continuity by solving a pressure equation. The calculated Cartesian velocity, pressure and temperature data are stored at the cell center; flux data are stored at the cell face. For the generalization to a complex geometry, the governing equations are transformed from physical coordinates $\vec{x} = (x, y, z)$ to logical/computational coordinates $\vec{\xi} = (\xi, \eta, \zeta)$ by means of boundary conforming transformation $\vec{x} = \vec{x}(\vec{\xi})$. More detail about the transformation can be found in Tafti [6]. μ_t is the dimensionless turbulent viscosity and is calculated by the dynamic Smagorinsky model in the LES framework [50 – 52]. The turbulent conductivity k_t is approximated as $k_t = \mu_t/0.5$ based on Moin *et al.* [53].

2.2 Fully Developed Assumption

The multi-rib configuration of the square duct experiment is modeled using a single rib under a fully developed flow and heat transfer assumption by setting periodic boundary conditions along the streamwise direction. For the fully developed assumptions, the governing equations are modified by incorporating mean streamwise pressure and temperature gradient terms in the momentum and energy equations, respectively. Here, the streamwise periodic modification with a constant heat flux at the wall is described briefly. More details about the implementation can be found in Patankar *et al.* [54] and Zhang *et al* [55].

Under the fully developed assumption, a wall friction velocity is used as a reference velocity and represented as below,

$$u_\tau^* = \sqrt{\frac{\tau_{w_{eq}}^*}{\rho_{ref}^*}} = \sqrt{\left(-\frac{\Delta P_x^*}{L_x^*}\right)\left(\frac{D_H^*}{4\rho^*}\right)} \tag{2.5}$$

where, $\tau^*_{w_{eq}}$ is the wall shear including form loss in the domain, ΔP^*_x is the mean pressure gradient in the flow direction, L^*_x is the periodic domain length, and D^*_H is the hydraulic diameter.

Due to the streamwise directional dependency of both the pressure and the temperature, the assumed streamwise periodicity of the domain requires the mean pressure gradient and temperature gradient to be separated from their fluctuating components. To do so, the mean gradients of the pressure and the temperature are calculated as below,

$$\beta^* = \frac{\Delta P^*_x}{L^*_x} \tag{2.6}$$

$$\gamma^* = \frac{\Omega^*_s \, q^*_w}{\rho^* C^*_p Q^*_x L^*_x} \tag{2.7}$$

where, Ω^*_s is heat transfer surface area, Q^*_x is the flow rate and q^*_w is the constant heat flux from the interfacial wall to the fluid region.

Then, the pressure and the temperature can be expressed with two separated terms as below,

$$P^*(\vec{x}, \mathrm{t}) = P^*_{ref} - \beta^* \cdot x^* + p^*(\vec{x}, \mathrm{t}) \tag{2.8}$$

$$T^*(\vec{x}, \mathrm{t}) = T^*_{ref} + \gamma^* \cdot x^* + \theta^*(\vec{x}, \mathrm{t}) \tag{2.9}$$

where, P^*_{ref} is the arbitrary reference pressure, p^* is the periodic pressure fluctuations, T^*_{ref} is the arbitrary reference temperature and θ^* is the periodic temperature fluctuations.

Using parametrizations in equation (2.1) and characteristic temperature $T^*_o = q^*_w D^*_h / k^*$, equation (2.8) and (2.9) are non-dimensionalzed as below,

$$P(\vec{x}, t) = -\beta x + p(\vec{x}, t) \tag{2.10}$$

$$T(\vec{x}, t) = \gamma x + \theta(\vec{x}, t) \tag{2.11}$$

Modified momentum and energy equations with the fully developed assumption can be done by substituting equation (2.10) and (2.11) into equation (2.3) and (2.4):

Momentum:

$$\frac{\partial \rho u_i}{\partial t} + \frac{\partial (\rho u_j u_i)}{\partial x_j} = -\frac{\partial p}{\partial x_i} + \frac{1}{Re_{ref}} \frac{\partial}{\partial x_j} \left[(\mu + \mu_t) \frac{\partial u_i}{\partial x_j} \right] + \beta \vec{e}_x \tag{2.12}$$

Energy:

$$\frac{\partial \rho \theta}{\partial t} + \frac{\partial (\rho u_j \theta)}{\partial x_j} = \frac{1}{C_p \cdot Re_{ref} \cdot Pr_{ref}} \frac{\partial}{\partial x_j} \left[(k + k_t) \frac{\partial \theta}{\partial x_j} \right] - \rho \gamma u_x \tag{2.13}$$

where $\gamma = \frac{\Omega_s \, q_w}{(Re \cdot Pr)_{ref} \rho C_p Q_x L_x}$

and $\beta = 1$.

$\beta \vec{e}_x$ is the mean pressure gradient source term that balances the form and the friction losses in the domain and $\rho \gamma u_x$ is the heat sink term that balances the energy added to the fluid domain from the constant heat flux at the wall.

2.3 Immersed Boundary Method

In this thesis, the Immersed Boundary Method (IBM) is implemented in a generalized coordinate system. The IBM introduced here is the extension of a scheme developed by Gilmanov and Sotiropoulos [56] to a curvilinear coordinate system on a non-staggered grid. For the basic framework of this method, the solid boundary is immersed into a background mesh that is employed with special treatments in the vicinity of the immersed solid surface. The major IBM implementation and conjugate heat transfer (CHT) boundary treatment are introduced in this chapter. More details about the IBM framework and methodology can be found in Nagendra et al. [57].

The major steps in the implementation are as follows: (1) identification of the location of the immersed surface and determination of fluid and solid nodes; fluid and solid nodes immediately adjacent to the IB surface are labelled as IB nodes (2) solving the governing equations at all nodes

in the domain except at the IB nodes, and (3) applying a special treatment to reflect the presence of an immersed surface at the IB nodes.

In the first step of the IBM scheme, a solid boundary surface is created with either line segments (two-dimensional grid) or triangular elements (three-dimensional grid). Then, the solid surface is immersed into the desired location of the structured background mesh, which has a fixed location as shown in Figure 2.1 (two-dimensional example).

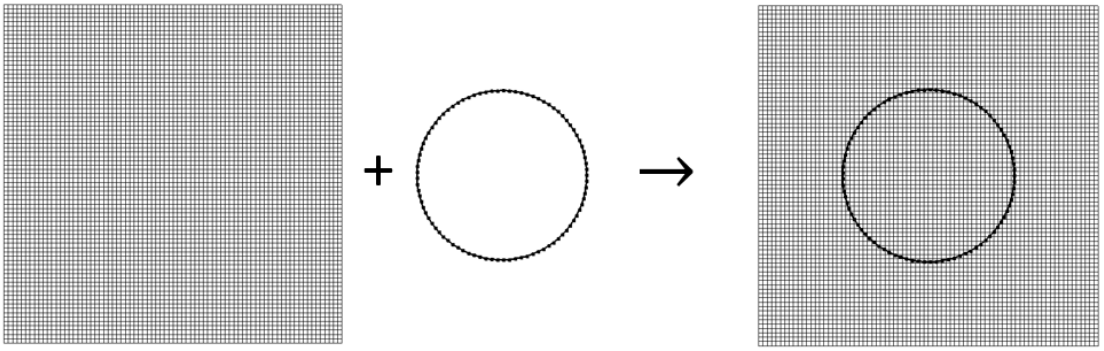

Figure 2.1: A two dimensional example of the background mesh (square domain with structured mesh) and the solid surface grid (circle with line segment).

Nodes near the immersed boundary (IB) are identified as either solid or fluid nodes in the background mesh by using a search-locate and interpolate (SLI) algorithm [58]. IB nodes, on the other hand, are nodes that lie in the immediate vicinity of the immersed boundary. For CHT simulations, since the temperature field is solved in both the fluid and solid regions, IB node assignment is necessary on either side of the immersed boundary as opposed to only on the fluid side for non-CHT simulations. Solid nodes that lie directly next to the immersed boundary are called solid IB nodes.

A 2D example of different node types for a CHT case is shown in Figure 2.2. The first set of nodes lying directly next to the immersed boundary are the fluid IB and solid IB nodes. All other

fluid nodes (and solid nodes, for energy equation) are affected by the presence of the immersed boundary through their interaction with the fluid (and solid) IB nodes.

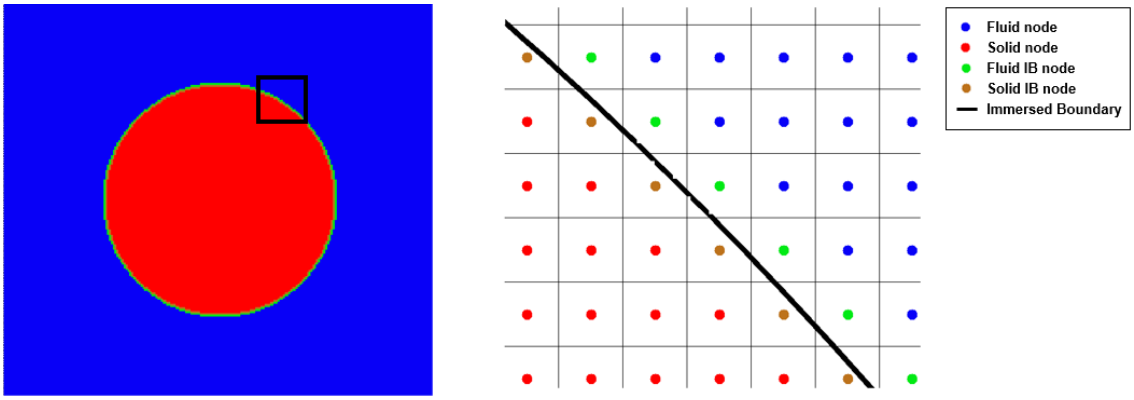

Figure 2.2 : Node types and the immersed boundary.

Once the node identification process is completed, the governing equations are solved on all fluid and solid nodes except the IB nodes which act as *de facto* boundary nodes. During the solution process, the IB nodes are continually updated based on the applied boundary condition at the IB surface. To reconstruct the solution at the IB nodes, probes that extend into the domain from the IB nodes are defined. Variables are interpolated at the probe locations using a tri-linear interpolation scheme, and these values are used in conjunction with the desired boundary condition at the immersed boundary to obtain the IB node values. For simulations involving conjugate heat transfer (CHT), the energy equation is solved in the fluid region as well as the solid region at the defined solid and fluid nodes in the domain, hence, probes are constructed on both the solid and fluid sides.

For CHT simulations, two boundary conditions are satisfied at the IB simultaneously – (1) a Dirichlet condition at the IB which ensures the continuity of the temperature field across the interface between the two media:

$$\theta^{f}_{wall} = \theta^{s}_{wall} \tag{2.14}$$

and (2) a Neumann condition at the wall location, which accounts for the balance of energy transferred across the interface:

$$-q''_{IB} = k_f \frac{\partial \theta}{\partial n}\Big|_{wall}^{f} = k_s \frac{\partial \theta}{\partial n}\Big|_{wall}^{s} \tag{2.15}$$

where, q''_{IB} is the heat flux at the immersed boundary, n is a surface normal direction, k_f and k_s are the thermal conductivities of fluid and solid, respectively. Here, the subscript *wall* denotes the IB surface. For every IB node (fluid or solid), information from the other side (solid or fluid) of the surface is required. Hence, additional "mirror" probes are defined at geometrical mirrored locations about the IB. Mirror probes are defined for all IB nodes (fluid and solid) as illustrated for a 2D example in Figure 2.3. The following procesure is for fluid IB nodes only, but exactly the same procedure is applied to solid IB nodes as well.

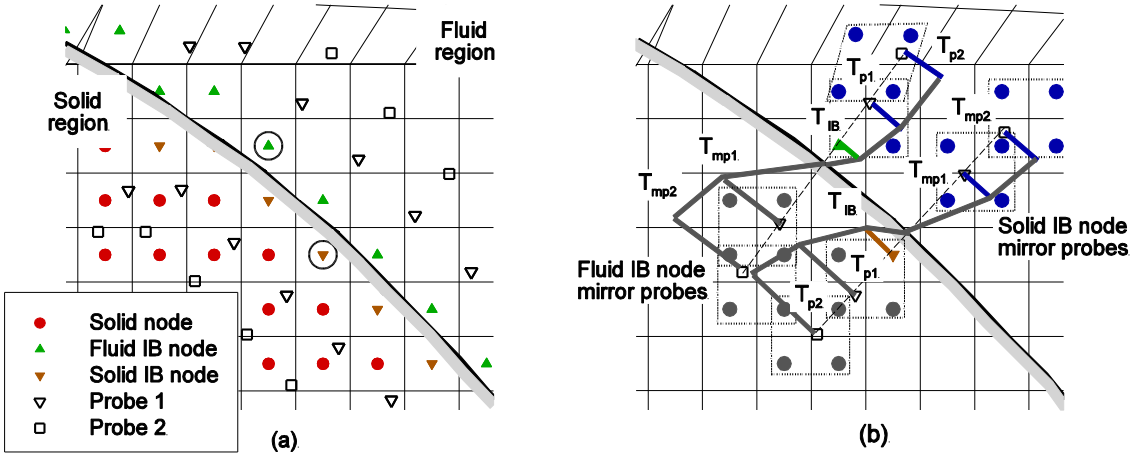

Figure 2.3: Conjugate heat transfer treatment with use of probes and mirror probes. Distances are measured from the immersed boundary, and the mirror probes mp1 and mp2 are located at the same distance as p1 and p2 (that is at d_{p1} and d_{p2}, respectively). The gray and the blue circles in (b) represent the interpolation nodes used in the solid and fluid regions, respectively [57].

The first condition used is the equality of heat flux across the fluid-solid interface. The gradients on the fluid and solid sides are obtained using Taylor series expansions of the IB probes and mirror probes, respectively. From the above equality, an expression for the IB temperature (*wall*) is obtained as:

$$\theta_{wall} = \frac{-d_{p2}^2\left(k_s\theta_{mp1} + k_f\theta_{p1}\right) + d_{p1}^2\left(k_s\theta_{mp2} + k_f\theta_{p2}\right)}{\left(d_{p1}^2 - d_{p2}^2\right)\left(k_f + k_s\right)} \tag{2.16}$$

Similar expression can be obtained for solid IB nodes by swapping k_f and k_s in the equation above. The value at the IB node can then be expressed in terms of the temperature values at the two probe locations and wall as:

$$\theta_{IB} = \frac{\begin{bmatrix} d_{IB}d_{p2}\left(d_{IB} - d_{p2}\right)\theta_{p1} + d_{IB}d_{p1}\left(d_{p1} - d_{IB}\right)\theta_{p2} \\ +\left(d_{IB} - d_{p1}\right)\left(d_{IB} - d_{p2}\right)\left(d_{p1} - d_{p2}\right)\theta_{wall} \end{bmatrix}}{d_{p1}d_{p2}\left(d_{p1} - d_{p2}\right)} \tag{2.17}$$

For the IBM-CHT simulation, the heat flux at the immersed boundary, $q_{IB}^{''}$, is used as a heat flux at the wall in the equation (2.7). To calculate this heat flux, the temperature gradient is calculated by constructing a probe normal to each surface element and the heat flux is calculated as follows, where $\theta_{p1}$is the tri-linear interpolated temperature at the probe location.

$$q_{IB}^{''} = -k_f * \frac{\theta_{p1} - \theta_{wall}}{d_{p1}} \tag{2.18}$$

2.4 Wall Modeled LES

Large Eddy Simulation (LES) has been widely used for turbulence simulations. Compared to Reynolds-Averaged Navier Stokes (RANS), LES is more accurate. LES computes the large and energy-carrying large structures while small scales are modeled using subgrid scale models [59]. However, as the Reynolds number increases, even the energy carrying turbulent structures in the

inner boundary layer reduce in scale inversely proportional to ~$Re^{3/4}$. In this case, the number of computational cells required to resolve the inner layer increase by ~Re^3 in three-dimensions [60]. To alleviate the high computational cost, the inner layer is modeled (instead of being resolved) by the use of LES wall functions. In this work, a zonal two-layer wall model is used. The detailed implementation of wall modeled LES (WMLES) and validation can be found in Patil and Tafti [61]. A brief summary is given in this section.

The zonal two-layer model with LES is framed by solving the set of simplified inner wall layer equations in an embedded virtual grid between the wall and the first off-wall grid ($y^+ < 50$), while the filtered Navier-Stokes equations are solved in the outer wall layer. The coupling between the inner and outer wall layers is performed by using the instantaneous outer flow velocity as a boundary condition to the inner wall layer. Then, the set of simplified equations is solved to compute the wall shear stress, which is used as a boundary condition in the solution of the outer layer equations at the first off-wall node.

The simplified tangential momentum transport equation is formulated using the local wall coordinate system (n, t) in the inner wall layer. By neglecting the convection and the time derivative terms, the equation is further simplified as shown in equation (2.19) with the boundary conditions $u_t = 0$ at the wall and $u_t = \left\|\vec{U}_t\right\|$ at the edge of the inner layer.

$$\frac{\partial}{\partial n}\left[(\mu + \mu_t)\frac{\partial u_t}{\partial n}\right] = \frac{\partial P}{\partial t} \tag{2.19}$$

where, n is the surface normal direction, *t* is the tangential direction.

The eddy-viscosity [62] is modeled in the inner layer as shown below,

$$\mu_t = \mu * \kappa * d^+(1 - e^{d^+/A})^2$$

$$d^+ = \frac{\rho u_\tau d}{u} \tag{2.20}$$

$$u_\tau = \sqrt{\|\tau_w\|/\rho}$$

where, κ is the von Karman constant, d is the normal distance from the wall to the first grid point, A is a constant equal to 19. The equation is solved iteratively for u_τ and τ_w using a tri-diagonal solver with a second-order central difference approximation.

From the solution of equation (2.19), the magnitude of tangential wall shear stress is obtained as below,

$$\|\tau_w\| = \mu \left.\frac{\partial u_t}{\partial n}\right|_{wall} \tag{2.21}$$

Then, equation (2.21) is decomposed into the respective directional components shown below,

$$\vec{\tau}_w = \|\tau_w\|\vec{t} = \|\tau_w\| t_x \vec{e}_x + \|\tau_w\| t_y \vec{e}_y + \|\tau_w\| t_z \vec{e}_z \tag{2.22}$$

where, $\vec{t}$ is the unit tangential vector and

$$\mu \left.\frac{\partial u_i}{\partial n}\right|_{wall} = \|\tau_w\| t_i \tag{2.23}$$

Using the calculated wall stress component above as a boundary condition, the discretized momentum equation can be solved at the first grid point off the wall.

For the zonal two layer heat transfer model, the energy equation with negligible advection and source terms is written as below,

$$\frac{\partial}{\partial x_j}\left[(k + k_t)\frac{\partial \theta}{\partial x_j}\right] = 0 \tag{2.24}$$

,where $k_t = \mu_t / Pr_t$

To solve equation (2.24), the closure model is required for the turbulent Prandtl number. The formulation of Kays [63] is used in the current investigation and expressed as below,

$$\frac{1}{Pr_t} = 0.58 + 0.22\left(\frac{\mu_t}{\mu}\right) - 0.0441\left(\frac{\mu_t}{\mu}\right)^2 \left\{1 - exp\left[\frac{-5.165}{\left(\frac{\mu_t}{\mu}\right)}\right]\right\} \tag{2.25}$$

Equation (2.24) is solved in the inner layer zonal mesh in the similar approach that the equation (2.19) is solved. The condition specified at the wall and the temperature at the first grid point off the wall are used as a boundary condition to solve equation (2.24). Two different types of boundary condition can be specified at the wall: (1) a Dirichlet and (2) a Neumann.

Dirichlet boundary condition is used when the temperature at the wall is specified. Equation (2.24) is solved in the inner layer to obtain the following heat flux at the wall:

$$q_w^{"} = -k\frac{d\theta}{dn}\Big|_{wall} \tag{2.26}$$

Then, the above heat flux is used as a boundary condition for the outer LES grid.

Neumann condition is used when the heat flux at the wall is specified. In this case, equation (2.24) is solved using the wall heat flux as a boundary condition to obtain inner layer temperature profile. Using the inner layer temperature profile, the wall temperature is calculated as below,

$$\theta_{wall} = \theta_{i2} + \frac{\Delta d}{(k + k_t)} \tag{2.27}$$

where, θ_{i2} is the temperature at the first gird off the wall and Δd is the non-dimensional distance between the wall and the first grid off the wall.

2.5 Conjugate Boundary Condition for Body Fitted Grid Method

To complement the IBM-LES-CHT calculations, additional calculations using a body-fitted grid are also performed (BFG-LES-CHT), in which a fully-coupled system of equations in the fluid and solid regions is assembled and solved together. This is slightly different from the coupled framework in IBM-LES-CHT that solves the fluid and solid equations separately and then couples

them through applying the conjugate boundary conditions at the solid and fluid IB nodes iteratively during each time step.

In the finite-volume procedure the solid-fluid interface lies at cell faces (Figure 2.4) and the definition of thermal conductivity at the interface becomes ambiguous. In this section, the concept of the effective thermal conductivity to satisfy the conjugate boundary condition at the solid-fluid interface is introduced. For the BFG-LES-CHT simulation, the conjugate boundary condition is applied at the fluid-solid cell interface by using an effective thermal conductivity.

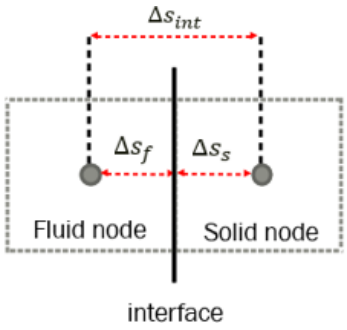

Figure 2.4: A fluid-solid interface. Δs_{int} is the distance between the fluid and solid node. Δs_f and Δs_s are distance between interface and the cell centroids (a fluid and a solid, respectively).

At the interface, below energy balance is satisfied,

$$-k_{eff}\left.\frac{d\theta}{ds}\right|_{interface} = -k_f\left.\frac{d\theta}{ds}\right|_{fluid} = -k_s\left.\frac{d\theta}{ds}\right|_{solid} \tag{2.28}$$

, where k_{eff} is the effective thermal conductivity of the interface, s, is the interface normal direction, k_f and k_s are the fluid and the solid thermal conductivity, respectively.

Based on the energy balance across the interface in equation (2.28) and the cell arrangement described in Figure 2.4, the effective thermal conductivity is determined as

below,

$$k_{eff} = \frac{\Delta s_{int} * k_f * k_s}{[\Delta s_f * k_s] + [\Delta s_s * k_f]} \tag{2.29}$$

and the heat flux across the interface is determined as below,

$$q''_{int} = -k_{eff} * \frac{\theta_f - \theta_s}{\Delta s_{int}} \tag{2.30}$$

For the BFG-LES-CHT with a fully developed assumption, the above interfacial heat flux is used to calculate the heat flux at the wall in the equation (2.7).

Chapter 3

IBM-LES Validation

In this chapter, the LES solver with the IBM framework is validated by simulating an internal cooling passage with a square rib configuration. The flow field and the turbulence intensity of the domain are compared with the experiments performed by Casarsa and Arts [6, 64, 65]. Furthermore, the IBM simulation is compared with the BFG simulation method which has been validated in previous papers [15, 49]. This validation is necessary prior to the conjugate heat transfer calculation to ensure that the effect of the turbulence is accurately predicted for the heat convection in the flow.

3.1 Problem Definition and Geometry

The geometry replicates the experiments of Casarsa and Arts [6] and Cukurel and Arts [32]. A square duct with ribs placed on only one wall is simulated at a nominal Reynolds number of 10,000 based on the hydraulic diameter and the mean flow velocity. The chosen Reynolds number is lower than the experimental Reynolds number to keep the cost of the simulations manageable since IBM generally requires a finer grid than body fitted grids. As a consequence, slightly higher heat transfer enhancement factors are expected [61, 68, 71]. The rib height to hydraulic diameter ratio is 0.3 and the pitch to rib height ratio is 10. The ribbed wall thickness is $0.33D_h$. Using the fully developed assumption along the streamwise direction, only a single rib is included in the computational domain.

Figures 3.1 (a) shows the computational domain. Figure 3.1 (b) shows the triangulated surface mesh containing 112,746 unstructured triangular elements on the ribbed wall which is the IB surface. Regions above and below the IB surface are considered as the fluid region and the solid

region, respectively. For BFG-LES, the solid region is not included in the calculation. For IBM-LES, the solid region is included but no calculations are done in the solid region. The top wall and sidewalls of the duct are treated in the body-fitted framework for both IBM-LES and BFG-LES. Figure 3.1 (c) shows the cell spacing distribution in the x, y, and z directions, respectively, of the background mesh. The background Cartesian mesh contains $224 \times 144 \times 96$ (~3 million) cells along the streamwise (x), wall-normal (y), and span-wise (z) directions, respectively. The background mesh cell size in the vicinity of the IB surface is chosen to be 2.5×10^{-4} non-dimensional units (y=0.33), which results in a n^+ value around 1, to adequately resolve the boundary layers. A wall-modeled LES with a zonal near-wall treatment strategy is used at the top and side walls of the background mesh, relaxing the n^+ requirement there. The IBM-LES calculation was run for a total of 55 non-dimensional time units out of which the last 25 time-units were used for obtaining the mean flow, turbulence, and thermal quantities.

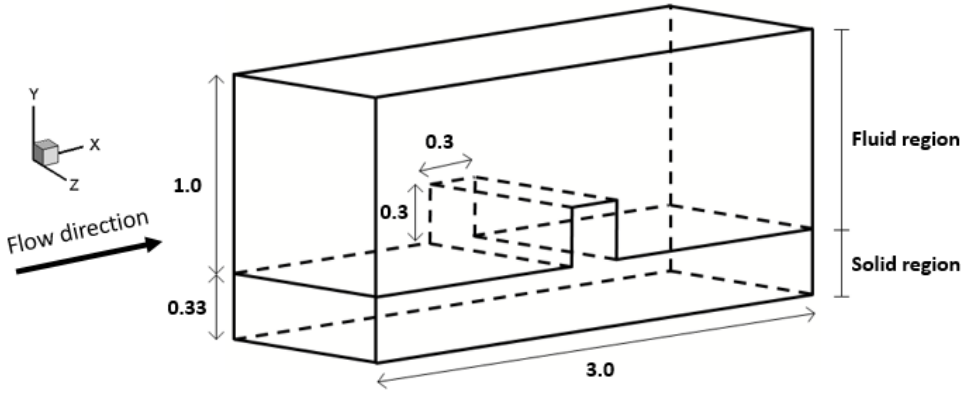

(a)

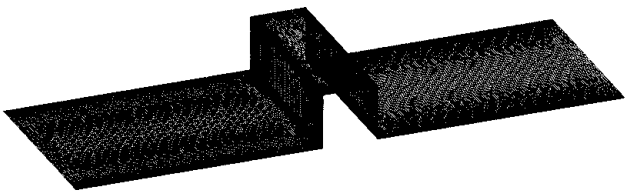

(b)

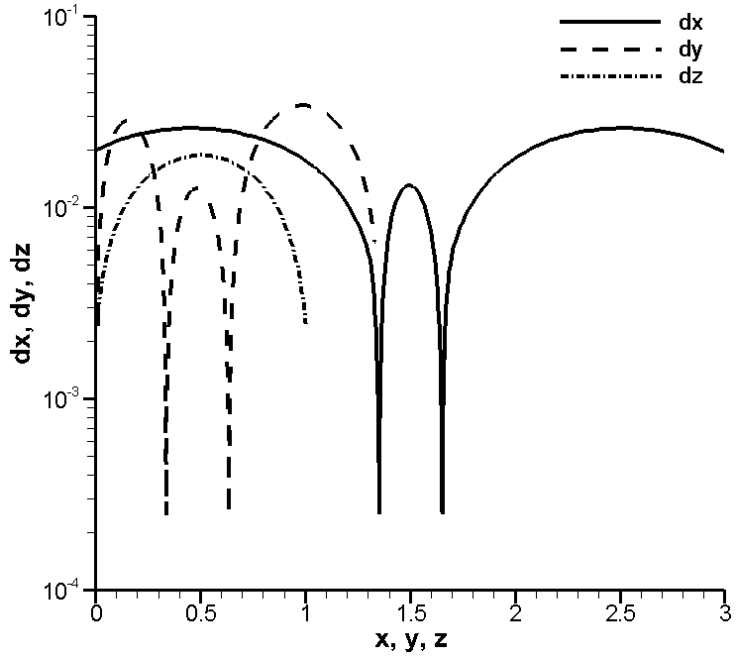

(c)

Figure 3.1: (a) Geometry, non-dimensionalized by hydraulic diameter (b) IB surface (c) Variation of x, y, and z spacing of the background mesh.

Figure 3.2 shows the computational domain and the cell spacing distribution in x, y, and z direction of the BFG simulation. Flow conditions and the overall computational cell size are the same as the IBM simulation. However, the solid region is not included in the BFG simulation, consequently, the computational domain contains $224 \times 114 \times 96$ (~2.5 million) cells. The BFG-LES simulation was run for a total of 49 non-dimensional time units out of which the last 22 time-units were used for obtaining the mean flow, turbulence, and thermal quantities.

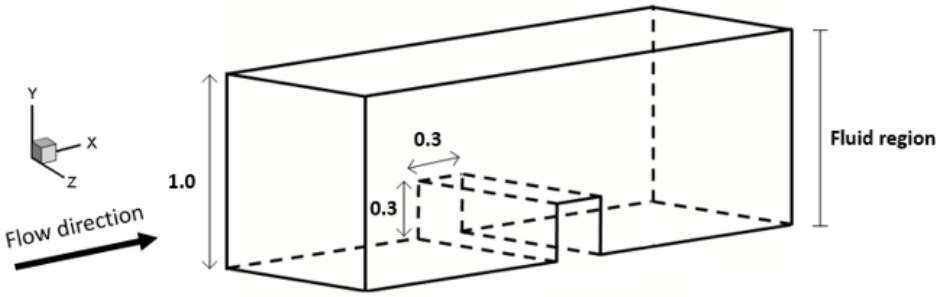

(a)

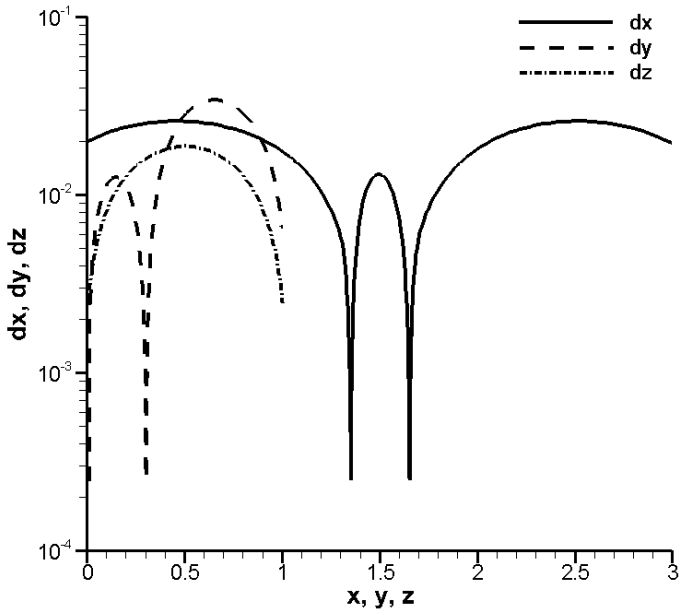

(b)

Figure 3.2: (a) Geometry of BFG simulation, non-dimensionalized by hydraulic diameter (b) Variation of x, y, and z spacing of the computational domain.

3.2 Results and Discussion

3.2.1 Flow Structure and Mean Flow Field Investigation

The predicted time-averaged velocity field is compared with the BFG prediction and the PIV experiment data by Casarsa and Arts [6]. Figure 3.3 shows the time-averaged velocity field in the symmetry plane of (a) the IBM prediction (b) the BFG prediction and (c) the experiment. In Figure

3.3 (a), there are four recirculation zones that are observed in the domain. The primary rib-induced recirculation zone (V4) in the wake of the rib extends about 3.5-4e behind the rib. This is supplemented by a much smaller counter-rotating sympathetic recirculation zone (V1) immediately behind the rib. After the reattachment of V4, a new boundary layer develops and is accelerated by the free stream until it impinges on the next rib, resulting in another recirculation zone (V3) at the bottom left corner of the next rib. In addition, a recirculation on the top of the rib is observed (V2). Table 3.1 shows the comparison of recirculation zone lengths between the IBM prediction and other comparative studies. The predicted recirculation length is measured using the same criteria as referred in the experiment [6]. As shown in Figure 3.3 and Table 3.1, the IBM captures all the major features of the flow and shows almost identical result with the BFG prediction. In addition, even though V1 length is slightly over predicted in both the IBM and the BFG predictions, other predicted recirculation lengths are in good agreement with the experimental measurement. Mainly, the comparison in V4, which is the largest recirculation zone, shows the difference less than 2 % between the both simulations and the experiment.

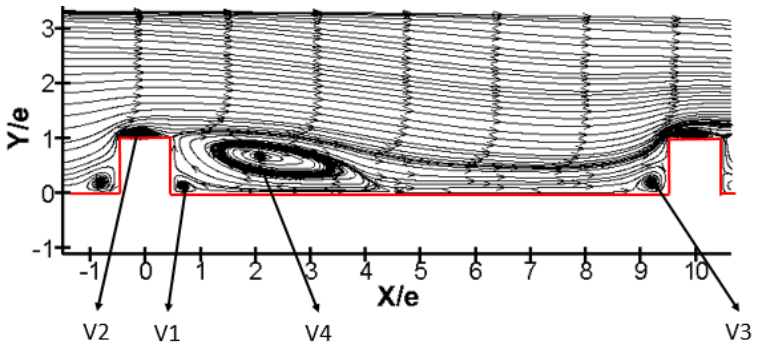

(a)

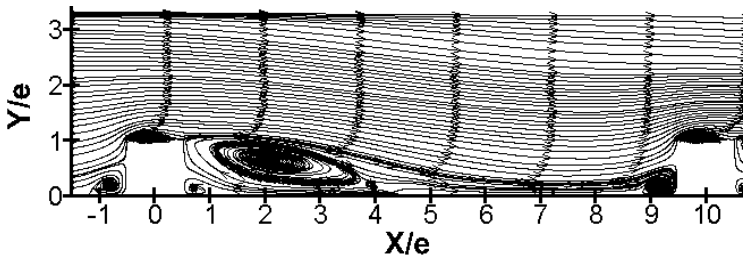

(b)

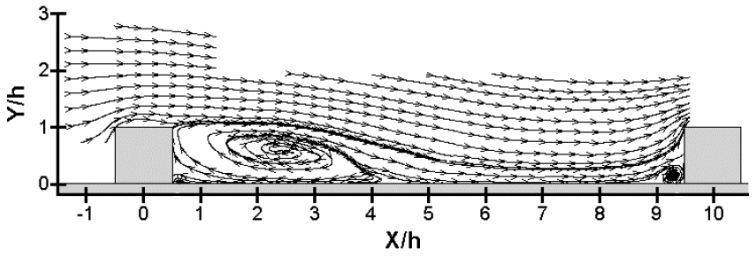

(c)

Figure 3.3: Time-averaged velocity field streamline on the symmetry plane of (a) IBM prediction (b) BFG prediction (c) Experiment [6], (h is equivalent to the rib height e).

Table 3.1: Recirculation zone size (*h* is equivalent to the rib height *e*)

	Zone V1	Zone V2	Zone V3	Zone V4
IBM Prediction	0.30	0.85	1.5	3.80
BFG Prediction	0.29	0.83	1.53	3.80
Experiment [6]	0.25	0.75	1.5	3.75

Cross-sectional secondary flow at two different locations, (*X/e* = 0 and 4.5) are shown in Figure 3.4 and 3.5. The shape and the location of the mean flow patterns are in good agreement between the IBM prediction and other comparative studies at *X/e* = 0. However, the small secondary flows at the corners of the duct are not captured in the experiment probably due to limited spatial resolution of the PIV technique. At *X/e* = 4.5, which is just downstream of the reattachment point,

the general streamline patterns are in good agreement. However, there is some discrepancies in the location of the structures.

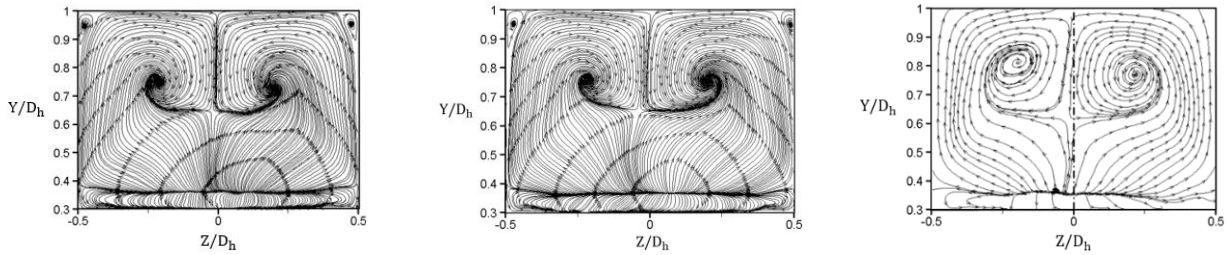

(a) **(b)** **(c)**

Figure 3.4: Streamline at the top of the rib (X/e = 0) by (a) IBM prediction (b) BFG prediction (c) Experiment [6].

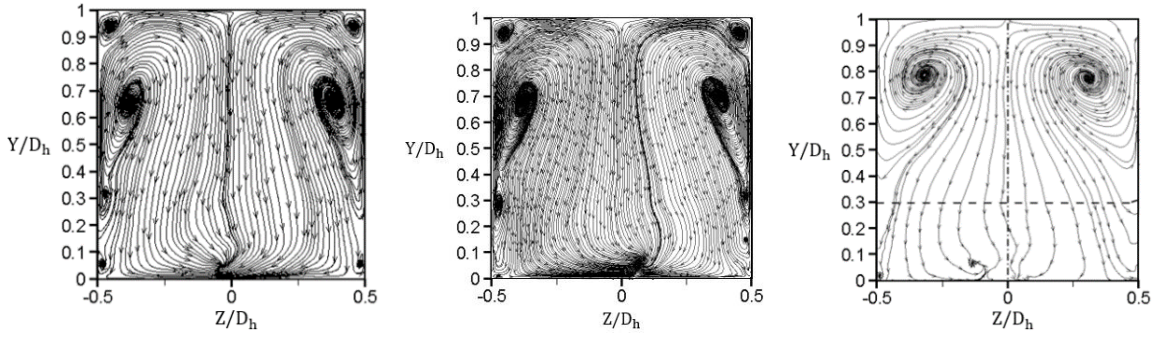

(a) **(b)** **(c)**

Figure 3.5: Streamline at the end of V4 recirculation (X/e = 4.5) by (a) IBM prediction (b) BFG prediction (c) Experiment [6].

3.2.2 Turbulence Field Investigation

Figure 3.6 – 3.10 show the time-averaged turbulence statistics at the symmetry plane from the IBM prediction, the BGF prediction and the experiment by Casarsa and Arts [64, 65]. In Figure 3.6, the streamwise turbulence intensity (*Urms*) plots from the IBM prediction matchs well with the BFG prediction and the experiment in the overall distribution of *Urms*. The maximum *Urms*

is observed in the separated shear layer at the leading edge of the rib, which is approximately 0.77, from all studies. A somewhat faster decay in peak magnitudes in the shear layer is predicted in both the IBM and the BFG simulations. This discrepancy between simulations and the experiment could be due to grid coarsening downstream of the rib as shown in Figure 3.1 (c) and 3.2 (b). However, the results near the rib show good agreement between simulations and the experiment in both Figure 3.6 and 3.7.

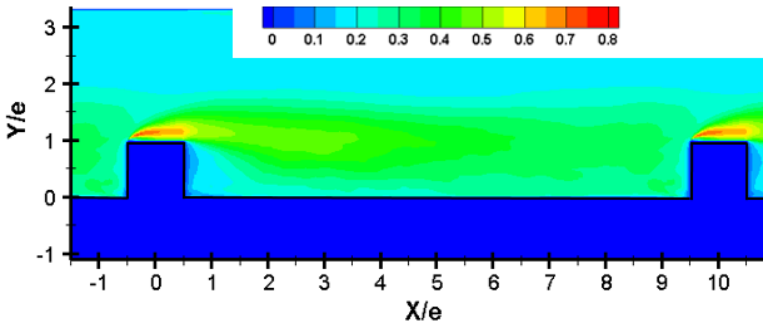

(a)

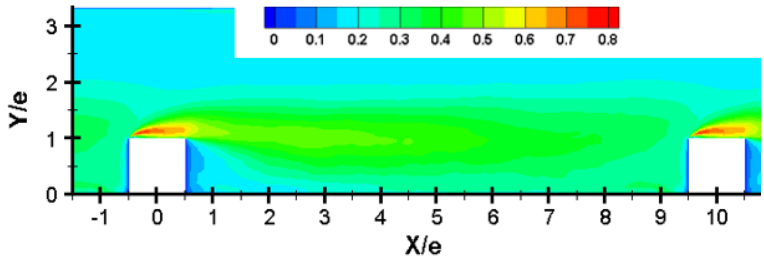

(b)

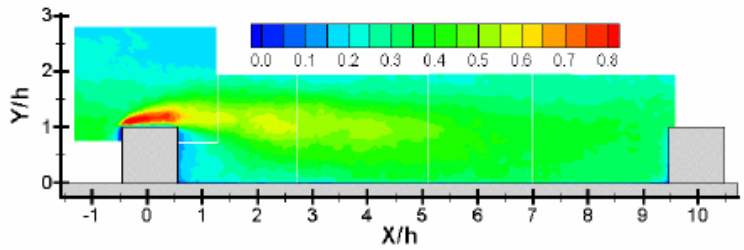

(c)

Figure 3.6: Time-averaged *Urms*, $\sqrt{\overline{u^2}/{U_b}^2}$, turbulence statistic on the symmetry plane. (a) IBM prediction (b) BFG prediction (c) Experiment [64], (*h* in experiment is equivalent to the rib height *e*).

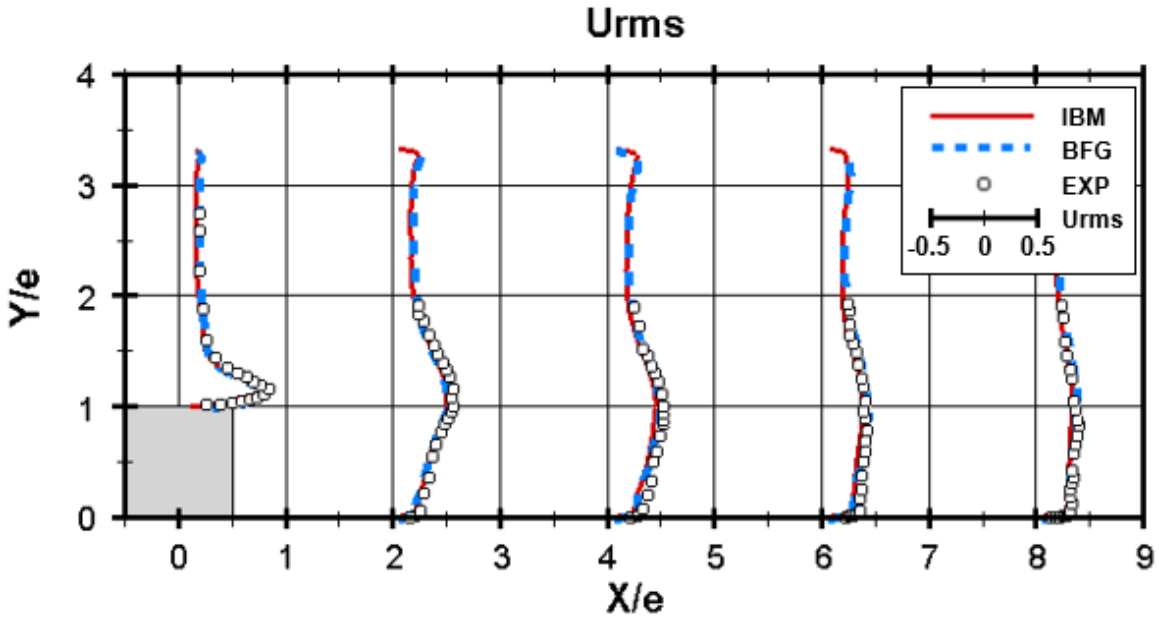

Figure 3.7: Urms plot along the wall normal (y) direction at the symmetry plane.

Figure 3.8 shows that vertical turbulence intensity (*Vrms*) distribution from IBM prediction agrees well with the BFG prediction and the experiment. In all cases, a maximum value of ~0.4 is reached in the separated shear layer between the ribs. Furthermore, Figure 3.9 shows that the distribution of *Vrms* by the IBM prediction downstream of the rib matches well with other comparative studies.

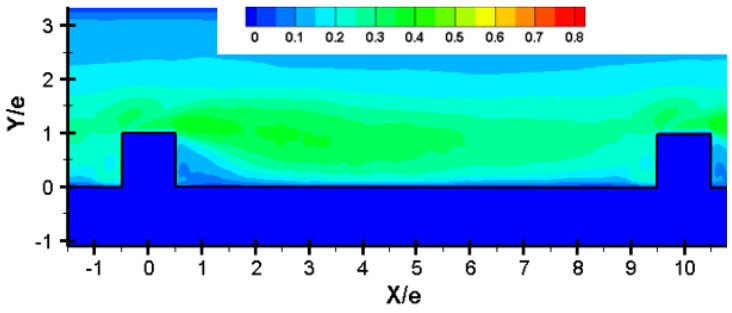

(a)

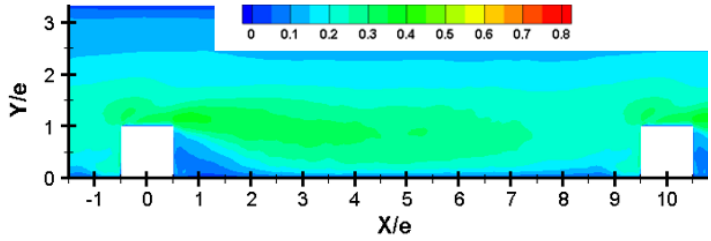

(b)

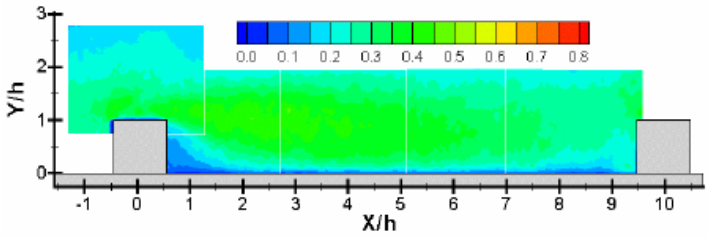

(c)

Figure 3.8: Time-averaged Vrms, $\sqrt{\overline{v^2}/{U_b}^2}$, turbulence statistic on the symmetry plane. (a) IBM prediction (b) BFG prediction (c) Experiment [64], (h in experiment is equivalent to the rib height e).

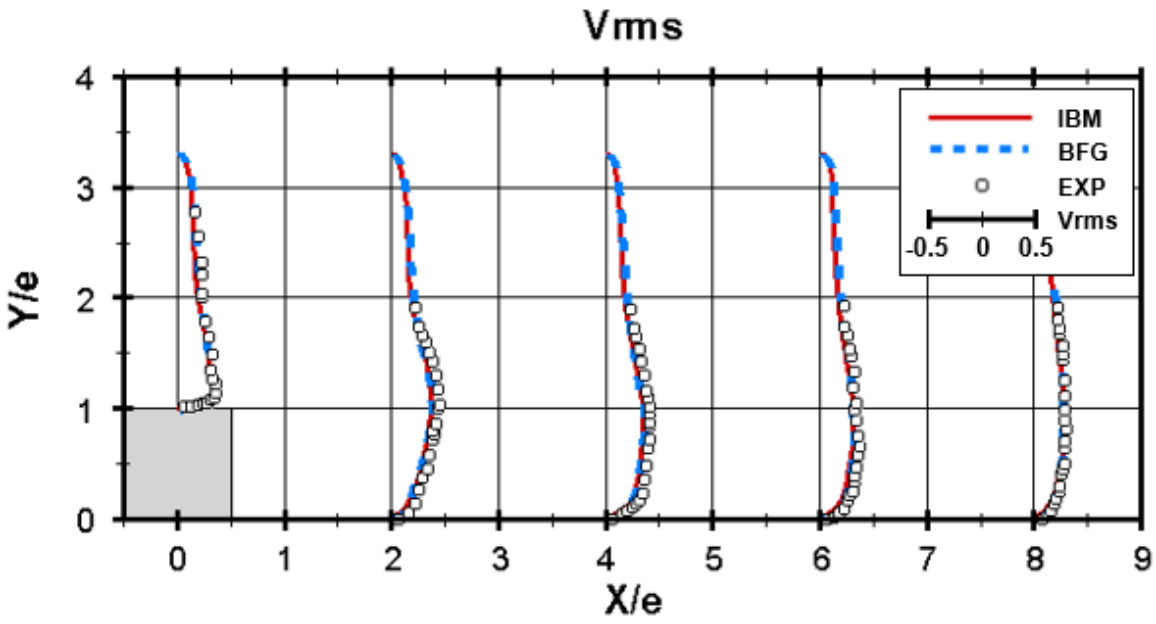

Figure 3.9: Vrms plot along the wall normal (y) direction at the symmetry plane.

Figure 3.10 shows turbulent shear stress distribution on the symmetry plane. The overall trend of the distribution is in good agreement between the IBM prediction and the comparative studies. The maximum shear stress is observed in the separated shear layer at the leading edge of the rib, which is around -0.18, from the IBM, BFG, and the experiment. In the region downstream of the rib (*X/e* = 2.5 ~ 3.5), the IBM predicts slightly higher shear stress than the BFG prediction. Similar to *Urms*, the predicted shear stress of both simulations in the separated shear layer decays faster than the experiment. Especially at *X/e* = 2 and 4,

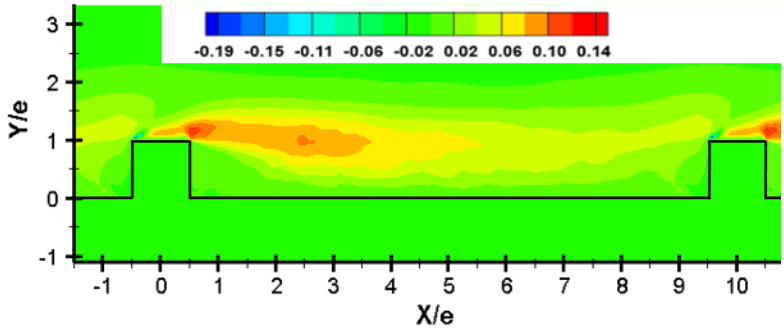

(a)

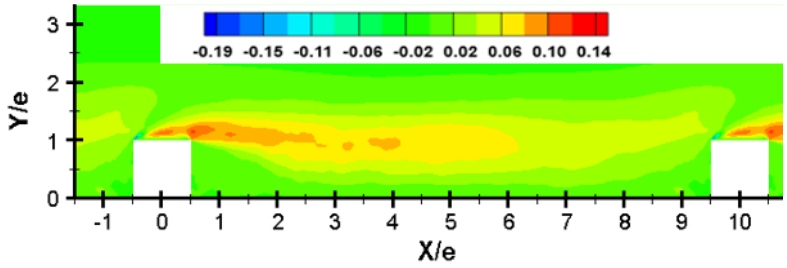

(b)

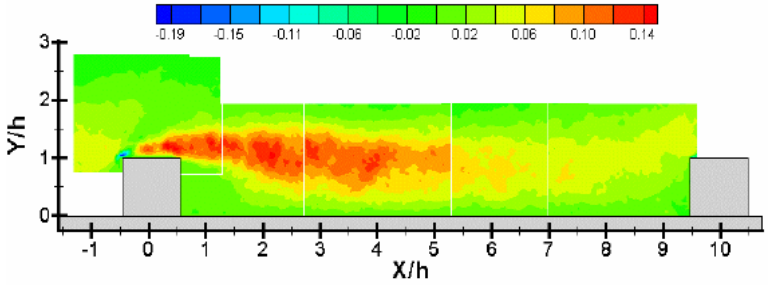

(c)

Figure 3.10: Time-averaged turbulent sheat stress, $-\overline{u'v'}/U_b^2$, on the symmetry plane. (a) IBM prediction (b) BFG prediction (c) Experiment [64], (h in experiment is equivalent to the rib height e).

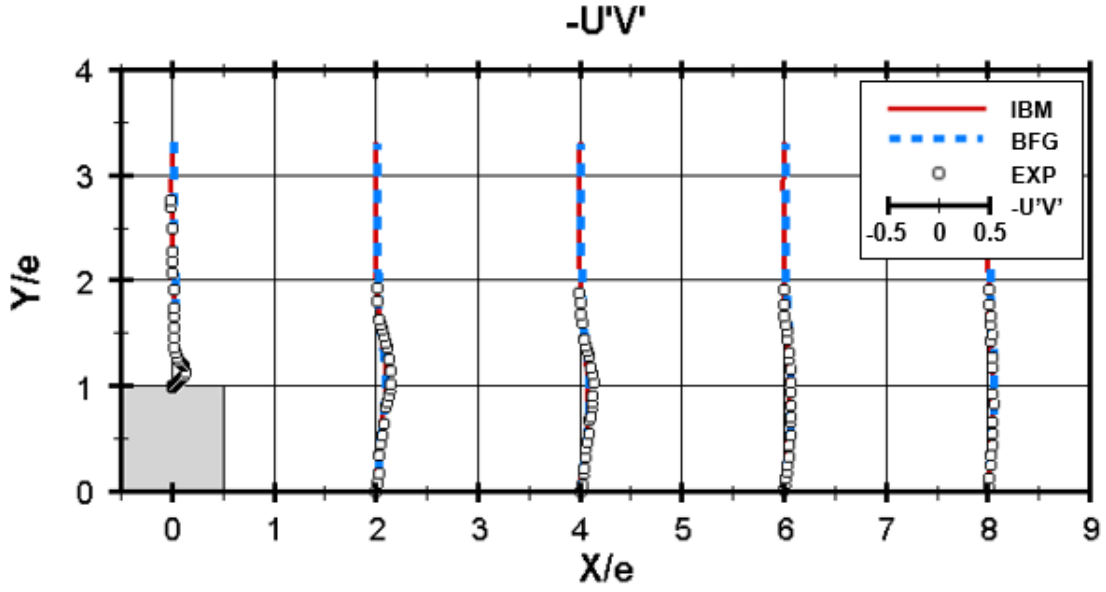

Figure 3.11: -U'V' plot along the wall normal (y) direction at the symmetry plane.

3.3 Conclusion

The flow field of the ribbed duct simulation using the IBM is investigated. The results are compared with the BFG prediction and PIV experiments. From the comparison, it is evident that the IBM captures the mean and secondary flow characteristic accurately for the square ribbed duct. Turbulence intensities predicted by the IBM agree well with the BFG prediction. However, both predictions show a somewhat faster decay of turbulence in the shear layer originating at the rib. This could be a result of grid coarsening downstream of the ribs. Overall, the predictions are in excellent agreement with experiments.

Chapter 4

IBM-CHT Validation

In this chapter, a conjugate boundary condition of the IBM is validated by simulating a two-dimensional developing laminar flow on a flat plate. The IBM prediction is compared with the BFG prediction and an analytical solution by Payvar [20]. This study is used to evaluate effects of the thermal conductivity ratio and the Biot number on conjugate heat transfer.

4.1 Problem Definition and Geometry

Figure 4.1 shows the physical model of the flat plate and the boundary conditions used in the simulation. The plate, which is a solid, has a constant temperature boundary condition at the bottom surface (T_b), and the convection in the fluid is coupled with the conduction in the solid at the interface between the fluid and solid regions. Reynolds number (Re_L) is set to 24,000 based on the plate length in the streamwise direction. The analytical solution [20] is obtained at high Prandtl number (Pr = 4.15) to approximate a linear velocity variation profile within the thermal boundary layer. To maintain one-dimensional heat conduction in the y-direction, the wall is made relatively thin compared to the length.

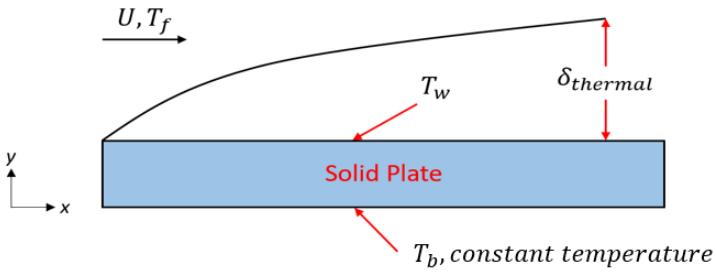

Figure 4.1: Physical model of the flat plate and the boundary condition

Figure 4.2 shows the computational domain with grid distribution. For an accurate thermal calculation, about 30 cells are placed within the thermal boundary layer. The IB surface represented by a line segment is immersed into the Cartesian background mesh as shown in Figure 4.2 (a). The background mesh contains 2163 × 377 (~0.8 million) cells in x- and y- direction, respectively. A constant temperature boundary condition is applied on the bottom surface of the background mesh, and the conjugate boundary condition is applied on the IB surface (interface) for the IBM simulation as discussed in chapter 2.3. For the BFG simulation, the computatioal domain replicates the background mesh of the IBM simulation. The solid region is defined where the solid and solid IB nodes are in the IBM simulation, then the CHT boundary condition is applied at the fluid-solid cell interface as described in chapter 2.5.

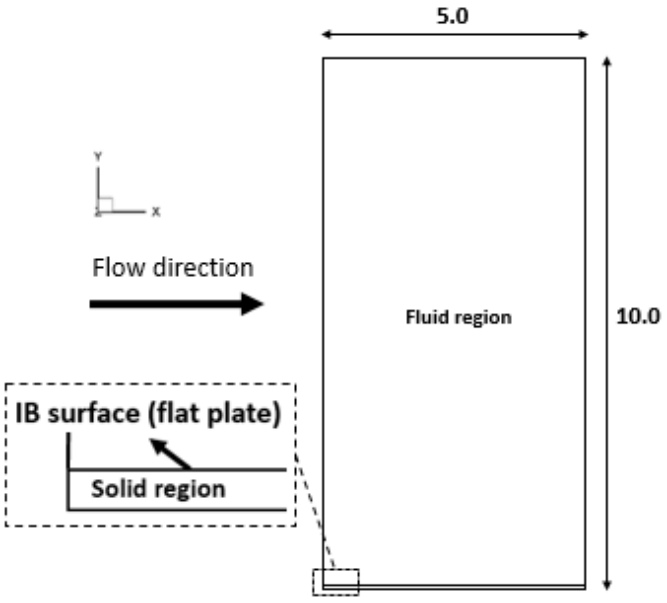

(a)

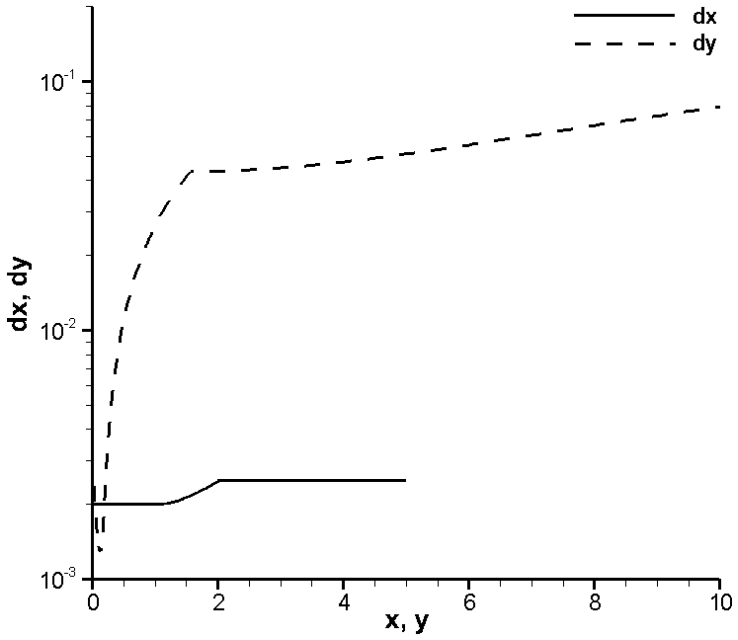

(b)

Figure 4.2: (a) Geometry and (b) Variation of x and y spacing of the background mesh.

Different Biot numbers are tested by using various solid to fluid conductivity ratios. The fluid conductivity is held constant, and the solid conductivity is changed to get the desired Biot number. Using a mean Nusselt number calculation of the external laminar flow ($\overline{Nu}_x = 0.664 Re_x^{1/2} Pr^{1/3}$) and the Biot number calculation ($Bi = \frac{h \times t}{k_f}$), a mean Biot number for the laminar flow on the flat plate is obstained as below,

$$Bi_{mean} = 0.664 * \frac{K_f}{K_s} \frac{t}{L} Re^{0.5} Pr^{\frac{1}{3}} \tag{4.1}$$

where, t is the thickness of the solid plate and L is the streamwise length of the plate.

The conductivity ratios and the Biot numbers used in the simulations are shown in Table 4.1. Each simulation was run until it reaches thermal steady-state using 10 processors. Table 4.2 summarizes the simulation wall clock time for different conductivity ratios using the IBM and BFG.

Table 4.1: Thermal conductivity ratios and the Biot numbers

k_s $(W/m \cdot K)$	k_f $(W/m \cdot K)$	K^* (k_s/k_f)	Bi_{mean}
0.0257	0.0257	1	3.3
0.128	0.0257	5	0.66
1.285	0.0257	50	0.066
2.57	0.0257	100	0.033
15.4	0.0257	600	0.0055

Table 4.2: Thermal conductivity ratios and the Biot numbers

K^* (k_s/k_f)	$IBM - CHT$ (hr)	$BFG - CHT$ (hr)
1	73	55
5	62	40
50	54	31
100	43	21
600	41	20

4.2 Results and Discussion

4.2.1 Local Conjugate Wall Temperature Comparison

For the analysis, the temperature of the fluid and the solid interface is non-dimensionalized as below,

$$\theta_{wall} = \frac{T_b - T_w}{T_b - T_f} \tag{4.2}$$

where, T_b is the temperature of the bottom surface of the solid region, T_w is the interface temperature between the fluid and the solid, and T_f is the temperature of flow field. (i.e. θ_{wall} value of zero indicates that the interface temperature is same as the solid temperature applied at the bottom of the wall.)

Figure 4.3 shows the non-dimensional temperature distribution at the interface. The interface temperature tends to zero as the solid to fluid conductivity ratio gets larger, i.e. as the Biot number gets smaller, the interface temperature gets closer to the bottom wall temperature of the solid region. This trend is expected based on the Biot number analysis introduced in Section 1.1.1. As the Biot number tends to zero, the resistance to conduction in the solid is less significant, consequently, the interface temperature tends to the constant bottom wall temperature of the solid region. The IBM prediction shows almost identical results with the BFG prediction. Furthermore, the comparison between the analytical result and the IBM prediction shows good agreement.

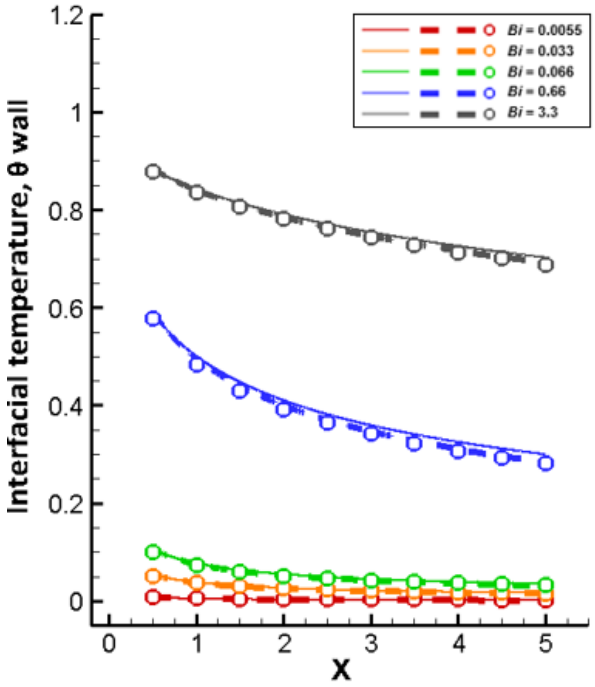

Figure 4.3: Fluid-solid interface non-dimensional temperature along the streamwise direction. Symbols, dashed lines and solid lines represent analytical, BFG and IBM results, respectively.

4.2.2 Local Nusselt Number Comparison

The local Nusselt number is presented in terms of the ratio of the conjugate to non-conjugate local Nusselt numbers.

$$Nu^* = \frac{Nu_x}{Nu_{x0}} \tag{4.3}$$

where, Nu_x is the conjugate local Nusselt number and Nu_{x0} is the non-conjugate local Nusselt number defined as

$$Nu_{x0} = \frac{h_x x}{k_f} = 0.332 Re_x^{\frac{1}{2}} Pr^{\frac{1}{3}}, \quad Pr > 0.6 \tag{4.4}$$

where, h_x is the local convection coefficient, x is streamwise location along the plate length, k_f is the fluid conductivity, and *Pr* is Prandtl number.

Figure 4.4 shows the local Nusselt number ratio variation along the streamwise direction. As the conductivity ratio gets larger, the local Nusselt number ratio tends to 1, i.e. as the Biot number tends to zero, the conjugate effect becomes less significant. The most significant changes in surface temperature and Nusselt number ratio are found when *Bi*=3.3 for *K**=1. The IBM slightly under predicts the local Nusselt number than what the BFG predicts at the Biot number of 0.66 and 3.3, whereas the IBM over predicts at the Biot number of 0.0055, 0.033 and 0.066. A larger discrepancy between the analytical solution and the IBM is observed near the leading edge of the plate than the trailing edge, which may be due to a thinner thermal boundary layer at the leading edge with less number of computational cells resolving the boundary layer. However, the difference between the analytical result and the IBM along the plate in both Figure 4.3 and 4.4 is no more than 4 %.

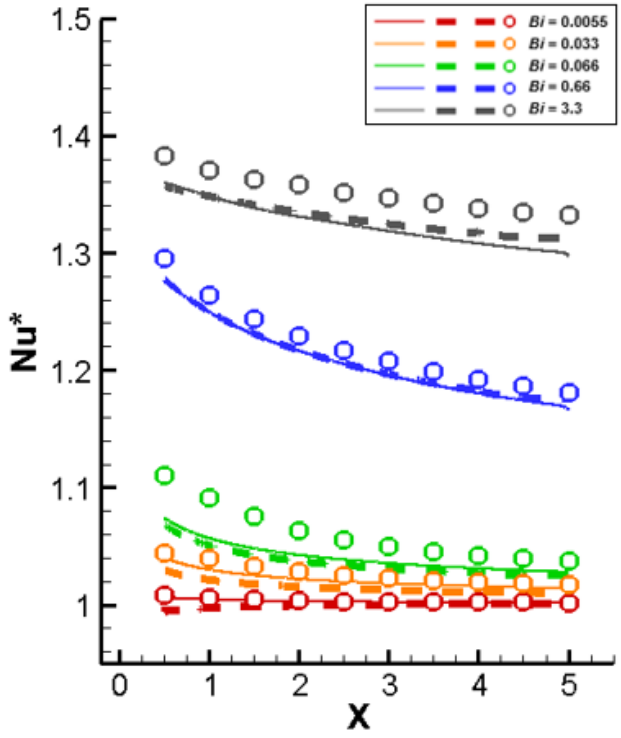

Figure 4.4: Nu* variation along the streamwise direction. Symbols, dashed lines and solid lines represent analytical, BFG and IBM results, respectively.

4.3 Conclusion

The conjugate boundary condition of the IBM is validated by simulating a two dimensional developing laminar flow on a flat plate. The fluid-solid interface temperature and the local Nusselt number along the streamwise direction are compared with the BFG prediction and the analytical solution. In two sets of comparisons, the IBM prediction shows almost identical result with the BFG prediction. The IBM slightly over predicts the interface temperature and under predicts the local Nusselt number compared to the analytical solution. However, the difference between the IBM and the analytical results shows no more than 4 % in both sets of comparisons.

Chapter 5

IBM-LES-CHT Validation

In this chapter, the IBM with a CHT boundary condition and fully developed assumptions is validated by simulating a canonical internal cooling passage of a turbine blade at Re = 10,000. In order to study the effect of the CHT boundary condition, an iso-flux boundary condition at the inner ribbed wall is also conducted. Furthermore, a use of an accelerated solid thermal diffusivity is introduced to compensate for the large time scale disparity between convection in fluid and diffusion in solid. Both the iso-flux and the CHT boundary conditions at the IB surface are simulated and compared with the BFG simulations, experiments by Cukurel and Art [32, 66] and other LES simulations by Scholl *et al*. [49, 67].

5.1 Problem Definition and Boundary Condition

5.1.1 Iso-flux Simulation

Figure 3.1 shows the ribbed duct geometry used for the simulations. The rib height to hydraulic diameter ratio is 0.3 and the pitch to rib height ratio is 10. The ribbed wall thickness, which is the solid region, is $0.33D_h$. For the IBM simulation with the iso-flux boundary condition (IBM-iso-flux), a constant heat flux is specified at the inner ribbed wall (IB surface) and the solid region is not solved during the calculation. Fully developed assumptions are applied along the streamwise direction and the adiabatic condition is applied at the side and the top walls of the duct. This calculation was run for 55 non-dimensional time units out of which the last 25 time-units were used for obtaining the mean flow, turbulence, and thermal quantities.

For the BFG-iso-flux simulation, the ribbed duct geometry does not include the solid region as shown in Figure 3.2, and a constant heat flux is applied at the ribbed wall. The grid size and the

geometry of the fluid computational domain are identical to that used for the IBM-iso-flux simulation. Fully developed assumptions are applied along the streamwise direction and the adiabatic condition is applied at the side and the top walls of the duct. The BFG-iso-flux calculation was run for 49 non-dimensional time units out of which the last 22 time-units were used for obtaining the mean flow, turbulence, and thermal quantities.

5.1.2 CHT Simulation

The geometry and the computational domain used for the IBM simulation with the CHT boundary condition (IBM-LES-CHT) are the same as what are used for the IBM-iso-flux simulation. For the IBM-LES-CHT simulation, a constant heat flux is applied at the outer ribbed wall that conducts through the solid wall. The CHT boundary condition is specified at the inner ribbed wall (IB surface) as described in Section 2.3.

IBM-LES-CHT simulation was run for 70 non-dimensional time units, out of which the last 25 were used to obtain the mean heat transfer quantities. This calculation was initiated without heat transfer for the first 15 non-dimensional time units to establish the flow field. Heat transfer was then activated with accelerated thermal diffusivity (Case 1) in the solid. When the fluctuating temperature reached a stationary state (after 25 non-dimensional time units), the solid properties were changed to Case 2 and the calculation was continued until another stationary state was achieved after 5 non-dimensional time units. At this stage, time-averaging was initiated to calculate the mean thermal quantities and the Nusselt number distribution on the rib surface. To investigate the effect of solid thermal diffusivity on predictions, Case 1 with the accelerated thermal diffusivity was also run together with Case 2 to obtain the mean thermal characteristics. The simulation time of the IBM-LES-CHT is summarized in Table 5.1

For the BFG-LES-CHT simulation, the computational domain replicates the background mesh of the IBM-LES-CHT simulation (Figure 3.1 c). The solid region is defined where the solid and solid IB nodes are in the IBM simulation, and the conjugate boundary condition is applied at the fluid-solid interface as described in Section 2.5. The same thermal calculation step is applied to the BFG-LES-CHT simulation as shown in Table 5.1. The BFG-LES-CHT simulation was run for 55 non-dimensional time units out of which the last 23 were used to obtain the mean heat transfer quantities.

In all simulations, the top and the side walls of the domain are adiabatic as in the simulation by Scholl *et al.* [49]. More geometrical details of the IBM and the BFG simulations can be found in Section 3.1.

Table 5.1: Simulation time of CHT case in non-dimensional time units

	Flow Establishment Period	Thermal Stationary-state Period	Thermal quantity averaging Period
IBM-LES-CHT	15	25 (Case 1) 30 (Case 2)	25
BFG-LES-CHT	12	20 (Case 1)	23

5.2 Treatment of Conjugate Heat Transfer

As described in Chapter 1, the Biot number determines how convection and conduction heat transfer are related. When the magnitude of resistance for the fluid convection and the solid conduction is the same (Bi∼1), the effect of convection and conduction coupling at the interface is significant. In the referenced experiment by Cukurel and Arts [32], a Biot number of ~1 is considered for the conjugate investigation, and the same value is maintained in the current simulations. In this way, the effect of conjugate boundary condition is preserved even though the Reynolds number between the experiments and the simulations are different (h is different because

of the difference in Reynolds number). This is achieved by modifying the thermal conductivity of the solid based on the estimated overall mean convection heat transfer coefficient and the target Biot number. It should be noted here that the estimation of the overall mean convection heat transfer coefficient on the ribbed wall for use in the Biot number is based on an augmentation factor of ~2.5 from the Dittus-Boelter correlation for a plain duct [68] at Re=10,000.

One challenge in solving fluid and solid domains simultaneously in a *coupled* framework is the large time scale disparity between the fluid and the solid. York [69] reported that the time scale for conduction in the solid was about five orders of magnitude larger than that for convection in the fluid for his conjugate simulation of the full C3X vane. In other words, the time scale of heat diffusion in the solid, $\tau_s = L_s^2/\alpha_s$, is much larger than the time scale required for convection in the fluid which is governed by turbulent time scales (interestingly the diffusion time scale in the fluid is of the same order of magnitude as that of stainless steel). This disparity in a steady state RANS framework can increase the condition number of the iteration matrix and make convergence difficult. In the time-dependent framework, however if time accuracy is desired in both the solid and fluid, the large time scale disparity results in large integration times for the heat to diffuse in the solid [70]. However, considerable simplification can result if this is not desired. In real engines, the transient startup would be of the order of seconds or at most minutes, while the steady state operation lasts at least an hour or more and in the case of land based gas turbines, 1000s of hours. All said and done, predicting the *spatial distribution of fluctuating quasi-steady state blade metal temperature* is of prime importance for durability predictions. In this endeavor, the convective heat transfer coefficient is the most significant parameter, which is best calculated by time-dependent LES.

Based on these observations, in the present study, artificial solid thermal properties are used to accelerate a heat diffusion within the solid region to compensate for the time scale disparity between convection and conduction. The initial transient is resolved by using a very high value of thermal diffusivity in the solid such that heat from the outer side of the ribbed wall diffuses to the inner wall in a short period of time. This is shown as Case 1 "Accelerated α_s" in Table 5.2. Once a statistically stationary thermal profile is reached in the solid, the thermal diffusivity, α_s is changed to reflect that of the actual solid (Case 2 in Table 5.2). Throughout these changes, the Biot number is kept at ~1, and only the density and the specific heat capacity of the solid are changed to get the desired thermal diffusivity. Table 1 lists the properties used in the simulations. It is noted that in order to maintain a Bi~1 and the correct α_s at Re=10,000, solid conductivity k_s is reduced to 1.254 W/m.K.

Table 5.2: Thermal properties of solid and Biot number

	Experiment (AISI 304 Stainless Steel)	Accelerated α_s (Case 1)	Physical α_s (Case 2)
Solid conductivity, k_s (W/m.K)	15	1.254	1.254
Density, ρ_s (kg/m^3)	8000	1.045	669
Specific heat capacity, C_{p_s} ($J/kg \cdot K$)	460	1.0	460
thermal diffusivity, α_s (m^2/s)	4.076 E-06	1.2	4.076 E-06
Biot number (*Bi*)	~1	~1	~1

5.3 Result and Discussion

The heat transfer results of the IBM simulations are investigated for the validation. The local Nusselt number for the IBM simulation is calculated as below,

$$Nu_x(\vec{x}) = \frac{h \cdot D_h}{k_f} = \frac{q''_{IB}}{\theta_{IB}(\vec{x}) - \theta_b} \tag{5.1}$$

where,

$$\theta_b = \frac{\int_{L_x} \left(\iint_{A_x} |U_x| \cdot \theta \cdot dA_x \right) dx}{\int_{L_x} \left(\iint_{A_x} |U_x| \cdot dA_x \right) dx} \tag{5.2}$$

The augmentation ratio is calculated based on the Dittus-Boelter correlation,

$$EF = \frac{Nu_x}{Nu_0} \tag{5.3}$$

where,

$$Nu_0 = 0.023 * Re^{0.8} * Pr^{0.4} \tag{5.4}$$

For a nominal *Re* =10,000, Nu_0 = 31.6.

5.3.1 Iso-flux Heat Transfer Prediction

Figure 5.1 shows the mean Nusselt number augmentation ratio (EF) of the rib front, top and back faces of the IBM-iso-flux and the BFG-iso-flux predictions. It is clearly seen that the IBM prediction agrees well with the BFG prediction. The highest augmentation (~7) is observed at the top of the rib front face as the flow impinges and accelerates over the top edge of the rib. Furthermore, the augmentation is small (0.5 - 2.5) at the back face of the rib due to the presence of the primary recirculation zone in the wake of the rib and resulting low turbulence intensity. Even though there is a slight difference in EF values between the IBM and the BFG predictions, the area-averaged EF in Table 5.3 shows the difference no more than 2% for all rib faces.

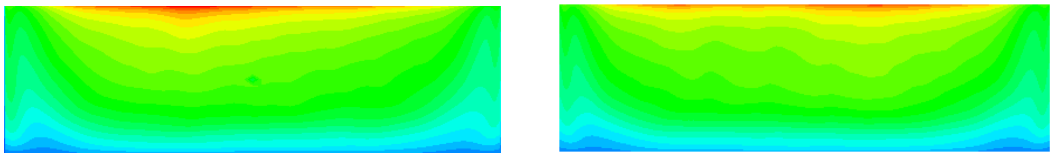

(a) Rib front face (b)

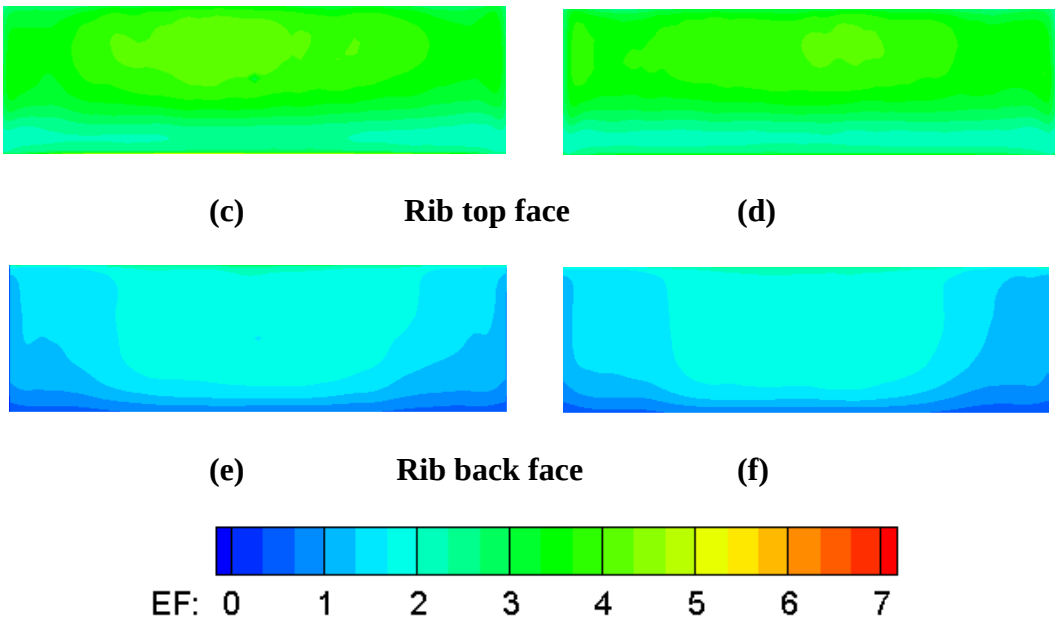

Figure 5.1: The mean Nusselt number augmentation ratio (EF) on the rib faces of the IBM (a), (c), (e) and the BFG (b), (d), (f) for the iso-flux case.

The EF on the symmetry plane by the IBM prediction is compared with the BFG prediction, the LES simulation result of Scholl *et al*. [67] and the experimental data by Cukurel and Arts [66] in Figure 5.2. The horizontal axis measures the surface distance including *a*-*b* (front face of the rib), *b*-*c* (top face of the rib), and *c*-*d* (back face of the rib).

The EF on the regions before and after the rib ($0 < S < 1.35$ and $2.25 < S < 3.6$) agree well among all four results in Figure 5.2. The heighest EF is observed at the leading edge of the rib ($S = 1.65$) for Scholl *et al*., the IBM and the BFG predictions, while this peak is absent in the experiment, probably due to a combination of non-ideal effects and lack of sufficient resolution. The computations also do not match with experiment at the front and the top faces of the rib. In the experiment, steady wide-band liquid crystal thermometry is used for the thermal measurement on the surface. In addition to the documented $\pm 4.5\%$ uncertainty in the measured enhancement factor [1], there are inherent downsides in measuring the time-varying turbulent temperature field

using a steady thermometry technique that can contribute to errors in the experiment. Scholl *et al*. [49] point out that these uncertainties can be especially pronounced near the edges of the rib where achieving high spatial resolution in experiments can be difficult.

The three LES computations compare quite favorably except at the front face of the rib, at which the current IBM and BFG show much higher augmentation values. The EF plot shows good agreement on the top and the back face of the rib for both simulations, whereas the EF of IBM and BFG on the front face of the rib is higher than documented by Scholl *et al*. The area-averaged mean difference in EF over the front face in Table 5.3, is about 20 %. The front face is where the flow directly impinges on the rib, resulting in high shear and heat transfer as the flow accelerates over the top of the rib. This is usually manifested as sharp gradients in temperature, requiring much finer grid resolution. Disagreement in the values between the current simulations and that of Scholl *et al*. are attributed to differences in the mesh resolution around the rib. In the current IBM and BFG, the largest n^+ in the vicinity of the rib is less than 1.0 over much of the rib face as shown in Figure 5.3, whereas it is approximately 6 in the setup of Scholl *et al.* [49, 67].

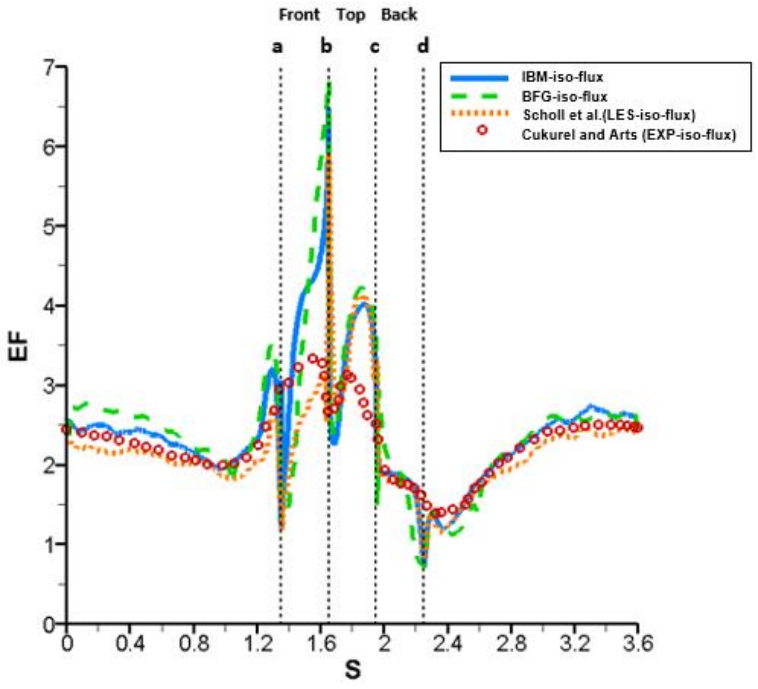

Figure 5.2: Convective heat transfer augmentation ratio on the symmetry plane comparison between the IBM (iso-flux) Prediction, the BFG prediction, experiment by Cukurel and Art [66], and simulation by Scholl et al. [67] along the ribbed wall surface including front, top, and back faces of the rib (front: a-b, top: b-c, back: c-d).

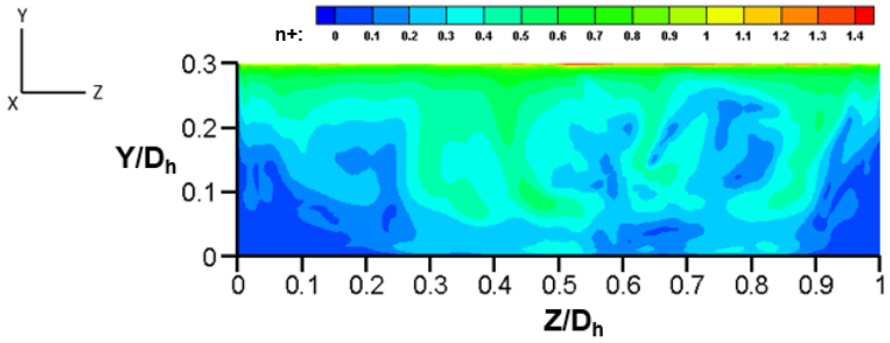

Figure 5.3: n^+ on the rib front face. n^+ is calculated using the wall normal distance of the first grid cell (Fluid IB node cell) and local shear stress values on the rib front face.

Table 5.3: Area-averaged EF on the rib for the iso-flux case

	Area-averaged EF			
	Front	Top	Back	Overall rib
IBM-LES-iso flux	3.50	3.23	1.55	2.76
BFG-LES-iso flux	3.52	3.22	1.58	2.75
Experiment-iso flux (Cukurel and Arts [66])	3.20	2.86	1.89	2.65
LES-iso flux simulation (Scholl *et al.*[67])	2.65	3.72	1.70	2.70

5.3.2 Effect of Solid Thermal Diffusivity

For *unsteady-CHT,* together with the Biot number, the thermal diffusivity in the solid (α_s) is also important. The Biot number bridges the fluid and solid domains and influences the mean wall temperature. On the other hand, the thermal diffusivity or Fourier number (*Fo*) in the solid region influences the fluctuations in wall temperature about this mean by controlling the rate of response of the wall temperature to temporal variations in the turbulent fluid temperatures. As $\alpha_s \uparrow$, the wall temperature and solid volume will respond on a short time scale to any change in fluid temperature, whereas $\alpha_s \downarrow$, it will respond slowly, on a longer time scale. The former exhibits low thermal inertia and low heat storage capacity, whereas the latter, high thermal inertia and high heat storage capacity to the extent that very short time scale temperature fluctuations will not even register in the solid.

Figure 5.4 shows the time evolution of temperature in the rib and the fluid at the indicated locations. For Case 1 with the accelerated α_s, the solid is very responsive to changes in the turbulent fluid temperature fluctuations and follows the fluid temperature closely. On the other

hand, for Case 2 with the correct diffusivity for stainless steel ($\alpha_s = 4.076 \times 10^{-6}\, m^2/s$), because of the high thermal inertia of the material, the solid temperature hardly responds to fluctuations in the fluid temperature but stays at a near constant value. The instantaneous heat transferred at the CHT surface in Figure 5.5, however, shows just the opposite trend in which Case 2 shows much larger fluctuations. This trend can be surmised from Figure 5.4 in which larger instantaneous temperature gradients exist between the solid surface and the fluid because the solid surface temperature does not respond to the fluid temperature as readily and quickly as it does in Case 1.

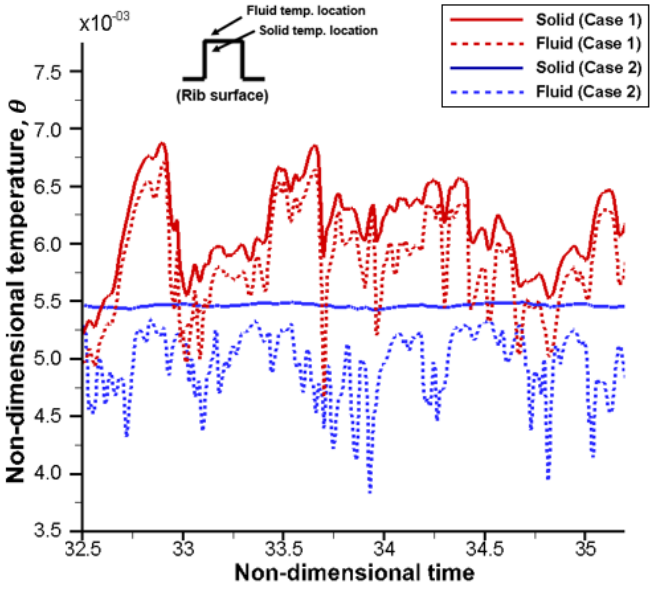

Figure 5.4: Instantaneous temperature variation at a single location in the solid rib and in adjoining fluid near the CHT surface.

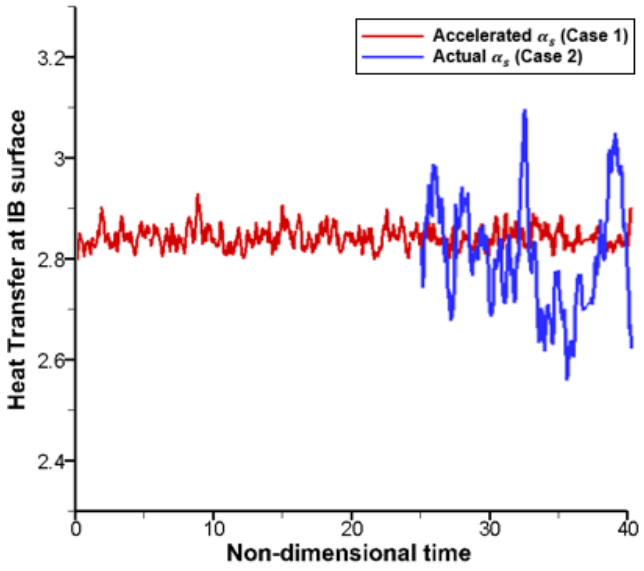

Figure 5.5: Instantaneous heat transfer at the full CHT surface. Time, t=0 is when heat transfer is activated.

Figure 5.6 shows the time variation of the overall area-averaged EF over the ribbed surface for both Case 1 and Case 2. The EF, which represents the Nusselt number, is a function of the instantaneous heat flux and the temperature gradient in the fluid at the CHT interface. Both Cases 1 and 2 show similar levels of instantaneous fluctuations. In Case 1, these fluctuations are manifested in the surface temperature, whereas in Case 2 they are manifested in the heat transferred. Thus both Case 1 and Case 2 show the same level of fluctuations in the heat transfer coefficient. It is noteworthy that in keeping with theoretical considerations on the transient importance of α_s, the mean EF for both cases only differ by 1 percent (2.34 for Case 1 and 2.36 for Case 2).

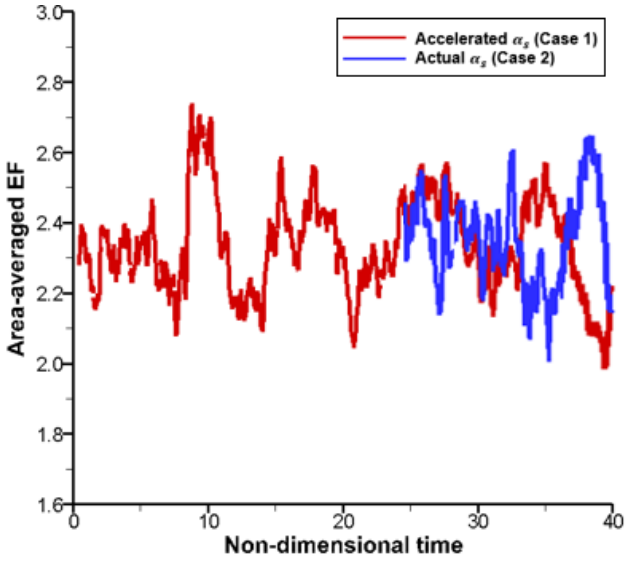

Figure 5.6: Area-averaged overall surface Nusselt number enhancement factor over the CHT-surface. Time, t=0 is when heat transfer is activated.

5.3.3 Conjugate Heat Transfer Predictions

Figure 5.7 shows the mean EF distribution of the rib by the IBM-LES-CHT and BFG-LES-CHT predictions using the accelerated solid thermal diffusivity (Case 1). The overall EF distribution of the IBM-LES-CHT agrees well with the BFG-LES-CHT. Furthermore, the EF is highest at the front face of the rib for both cases due to the flow impingement. Even though Table 5.4 shows that the area-averaged EF at the front and the top faces are under predicted and over predicted at the back face by the IBM, the comparisons on all faces show the differences within 5%. These differences are most probably statistical in nature.

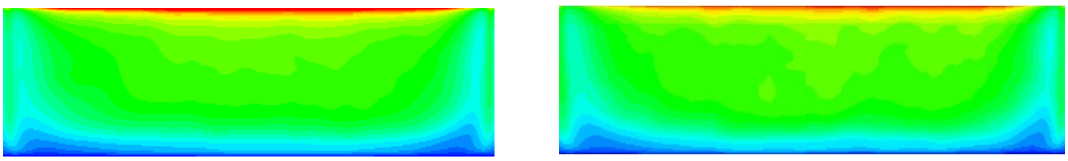

(a) Rib front face (b)

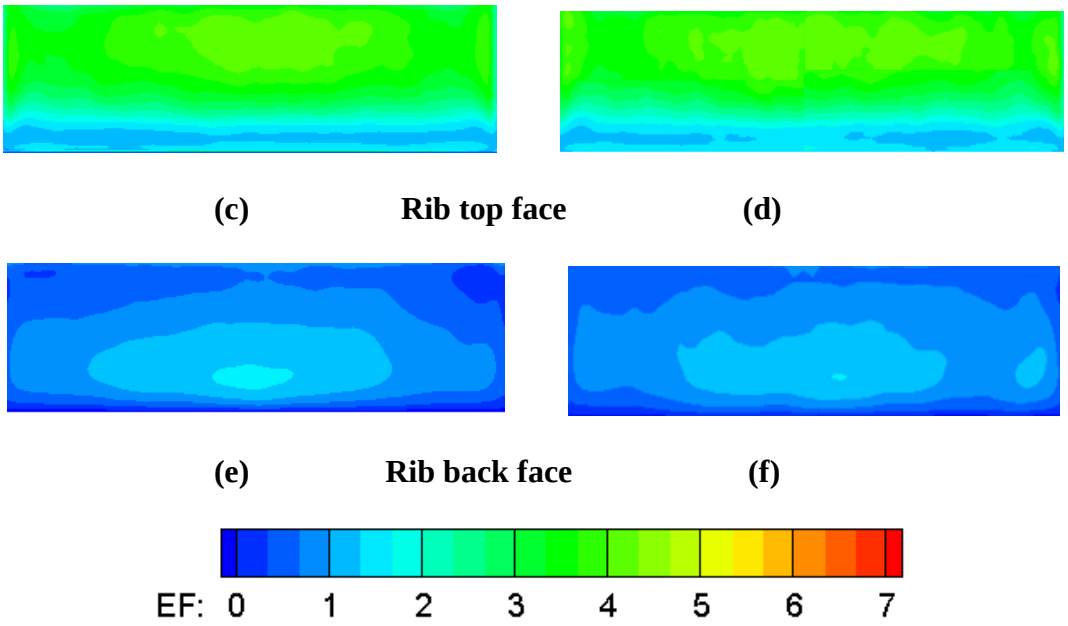

Figure 5.7: The mean Nusselt number augmentation ratio (EF) on the rib faces of the IBM (a), (c), (e) and the BFG (b), (d), (f) for the CHT case.

Figure 5.8 shows the comparison of the local mean Nusselt number augmentation ratio between the IBM-LES-CHT and BFG-LES-CHT predictions at the center plane. The IBM-LES-CHT matches well with the BFG-LES-CHT in the region before and after the rib, whereas the IBM-LES-CHT marginally over predicts the EF than the BFG-LES-CHT prediction at the rib region.

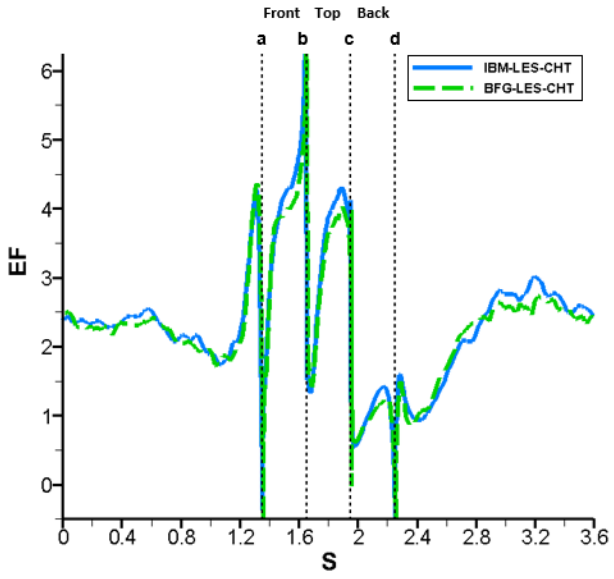

Figure 5.8: Comparison of conjugate augmentation ratio on the symmetry plane between IBM-LES-CHT prediction and BFG-LES-CHT prediction along the ribbed wall surface including front, top, and back faces of the rib (front: a-b, top: b-c, back: c-d).

Figure 5.9 shows the comparison of the local mean Nusselt number augmentation ratio between the two IBM-LES-CHT predictions (Case 1 and 2) and the purely convective heat transfer case (IBM-iso-flux) at the duct centerline to highlight differences between the three sets of calculations. It is found that the use of the accelerated and correct solid thermal diffusivities (Case 1 and 2) does not affect the mean distribution of the enhancement factor. There are small differences on the rib faces and in the reattachment region which can be attributed to statistical differences. In comparing the CHT cases and iso-flux boundary condition case, the major differences occur in the vicinity of the rib. It is noticeable that at points *a* and *d* in Figure 5.9, negative EF values are calculated in a very small region which indicates that the mean local flow temperature is higher than the rib corner temperature. This inverse heat flux phenomenon can be explained by observing the secondary recirculation zones (V1 and V3) generated near the bottom corners of the rib (Figure 3.3). These eddies could, in the mean, pick up heat from the bottom wall

which is typically at a higher temperature than the rib surface, and transfer that heat back into the front and back corners of the rib which are at a lower temperature. IBM-LES-CHT also predicts slightly higher EF in the reattachment zone.

Another major difference occurs at the back face of the rib ($1.95 < S < 2.25$). The difference is more evident in Table 5.4, which shows the area-averaged EF on each face of the rib. The EF of both IBM-LES-CHT predictions are lower than iso-flux prediction by more than 40 % at the back face. The large recirculation zone (V4), near the back face, generates a low momentum region with reverse flow. Due to this large recirculation zone, the heat transfer on the back face is relatively lower than that of other regions. The uniform heat flux applied at the back face of the rib for iso-flux prediction leads to a relatively high EF, whereas, the heat flux in the conjugate case is less because of the conduction resistance of the solid.

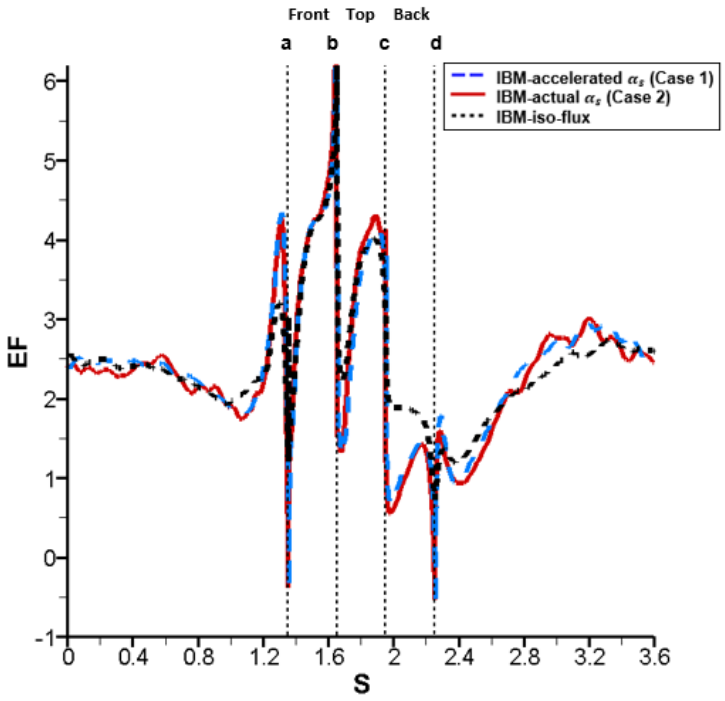

Figure 5.9: Comparison of conjugate and convective augmentation ratio on the symmetry plane along the ribbed wall surface including front, top, and back faces of the rib (front: a-b, top: b-c, back: c-d).

Figure 5.10 shows the comparison between IBM-LES-CHT predictions, the CHT experiment by Cukurel and Arts [32], and the LES-CHT simulation by Scholl *et al.*[49]. The overall trend in the EF plots are similar between the different studies, however, EF of IBM-LES-CHT predictions are higher than the experiments and the LES-CHT simulation of Scholl *et al.*[49] at the front face of the rib ($1.35 < S < 1.65$). Further, at point *b*, which is the leading edge of the top face, high EF is not observed in other studies. These trends are also seen in Figure 5.2 for iso-flux heat transfer. As mentioned earlier, this could be due to the limitation of the experimental spatial resolution and less number of computational cells used in the simulation by Scholl *et al.* [49].

To add further corroboration to the heat transfer result at the rib front face by the IBM-LES-CHT prediction, an internal LES-CHT study at Von Karmann Institute (VKI) by Benocci, based

on the current conjugate test case is also shown in Figure 5.10. This LES-CHT data is obtained from the experimental paper by Cukurel and Arts [49]. The EF trend of Benocci is similar to what the IBM-LES-CHT shows. Benocci has a higher EF at the front face of the rib than that shown by Scholl et al. and Cukurel and Arts. Furthermore, a high peak in EF is also observed at the leading edge of the rib (point *b*) from the results of Benocci. All results agree reasonably well on the top and the back faces of the rib. However, the trend predicted by the present CHT shows that EF increases traversing from *c* to *d* whereas the experiment [32] and past computations of Scholl *et al*. [49] show a somewhat opposite trend. It is observed that the current CHT simulations (both IBM and BFG) show a trend opposite to the iso-flux case, whereas, the previous experiments and predictions show the same trend as an iso-flux case. Similar to the front face of the rib, the heightened sensitivity to CHT in the current simulations could be a result of finer grid resolution in the vicinity of the rib

Table 5.4 summarizes the area-averaged EF of the rib. The area-averaged EF of IBM-LES-CHT predictions of the top and the back rib surface show good agreement with experiment, whereas there are differences when comparing to the simulations by Scholl *et al*.[49]. In addition, it is noteworthy that the area-averaged EF of the two IBM-LES-CHT predictions for all rib faces only differ by ~1 percent, as can be seen in Table 5.4.

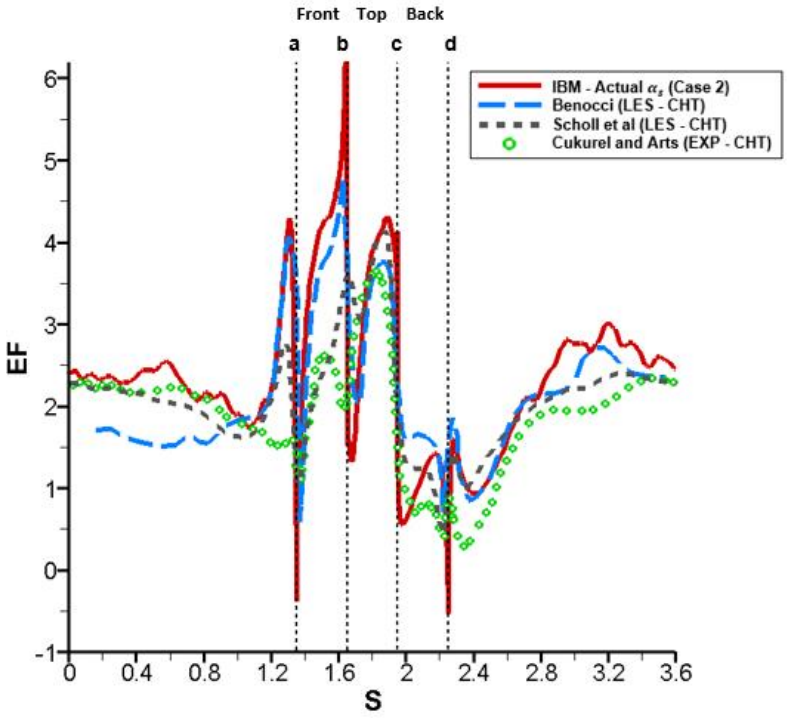

Figure 5.10: Comparison of conjugate augmentation ratio on the symmetry plane between IBM-LES-CHT prediction, experiment by Cukurel and Art [32], and simulation by Scholl et al. [49] along the ribbed wall surface including front, top, and back faces of the rib (front: a-b, top: b-c, back: c-d).

Table 5.4: Area-averaged EF on the rib for the CHT case

Area-averaged EF				
	Front	Top	Back	Overall rib
IBM - iso flux	3.50	3.23	1.55	2.76
Accelerated IBM-LES-CHT (Case 1)	3.25	3.04	0.86	2.36
Actual IBM-LES-CHT (Case 2)	3.24	3.07	0.86	2.34
Accelerated BFG-LES-CHT (Case 1)	3.35	3.10	0.82	2.40
Experiment-CHT (Cukurel and Arts [32])	2.34	2.99	0.86	2.07
LES-CHT simulation (Scholl *et al.*[49])	2.28	3.59	1.18	2.34

5.4 Conclusion

Iso-flux and conjugate heat transfer calculations are performed in a ribbed duct. The local Nusselt number augmentation ratio (EF) of both IBM-LES (iso-flux) and IBM-LES-CHT simulations are compared with the respective BFG-LES simulations, past experiments and LES simulations. Furthermore within the framework of a strongly-coupled CHT treatment, a method to eliminate the large computational time required to resolve the slow time scale of heat conduction in the blade material is proposed and validated. An artificially high solid thermal diffusivity is used initially to accelerate heat conduction in the solid followed by the use of the correct physical properties. It is shown that the mean heat transfer coefficient is independent of the solid thermal diffusivity as long as the same Biot number is maintained.

The comparison between the IBM-LES and the BFG-LES shows almost identical predictions of local EF and the area-averaged EF at the rib. The local EF at the top and the back faces of the rib by the LES-iso-flux simulation by Scholl *et al*. agrees well with current IBM-LES prediction, whereas the mean EF at the front face deviates by 20 %. This discrepancy could be due to coarse mesh resolution in the rib region; the largest n^+ value is around six in the setup of Scholl *et al*., whereas it is less than one in the current IBM simulation. The comparison with the iso-flux experiment shows that the EF at the front and the top faces of the rib from the experiment is lower than the EF predicted by the IBM-LES and BFG-LES.

For CHT, the solid temperature at the rib leading edge is investigated at two different solid thermal diffusivities (Case 1-accelerated and Case 2-physical). It is shown that the solid temperature in Case 1, which has a high solid thermal diffusivity, is more responsive to the fluid temperature fluctuations than Case 2 with a low solid thermal diffusivity. Conversely, Case 2 exhibits much larger fluctuations in heat flux than Case 1. However, it is noteworthy that the mean

heat transfer coefficient of both cases at steady state or stationary conditions only differed by 1 percent.

The comparison between the IBM-LES-CHT and the BFG-LES-CHT shows good agreement. However, the EF at the rib front face from both the LES-CHT simulation by Scholl *et al*. and the CHT experiment are much less than the EF predicted by the IBM-LES-CHT. On the other hand, the EF trend at the rib front face by the internal LES-CHT study at VKI by Benocci is similar to what the IBM-LES-CHT shows. The IBM-LES-CHT mean EF results on the top and the back faces of the rib at the symmetry plane agree reasonably well with past studies, however, the EF trend on the back face of the rib predicted by the IBM-LES-CHT shows a trend opposite to that of the simulation by Scholl *et el*. and the CHT experiment.

Although there are some discrepancies between the IBM-LES-CHT and other past studies, the comparison between the CHT and the iso-flux cases in each numerical and experimental studies commonly shows that the EF at the back face of the rib from the CHT case is lower than the EF from the iso-flux case by more than 40 %. This large difference is likely due to the conduction resistance of the solid that causes the heat flux in the conjugate case to be less. This conjugate effect is amplified at the back face of the rib, which has a large recirculating flow behind it.

Chapter 6

Summary and Conclusion

In this thesis, a strongly coupled conjugate heat transfer (CHT) simulation in a ribbed cooling passage with fully developed assumptions is evaluated using a LES solver with the immersed boundary method (IBM). In the IBM framework, the solid surface is immersed into a background volume mesh. However, the immersed geometry is not resolved exactly as it is in the body fitted grid (BFG); consequently, a fine mesh is required to determine the immersed geometry accurately. To reduce a grid requirement of the IBM simulation, fully developed assumptions along the streamwise direction and wall modeled LES (WMLES) are used in this study. For the conjugate simulation, both a Dirichlet (continuity in temperature) and a Neumann condition (continuity in heat flux) are specified at the immersed surface.

In Chapter 3, the LES solver with the IBM framework is validated by simulating a ribbed internal cooling passage at Re = 10,000. The flow field and the turbulence intensities predicted by the IBM are compared with the BFG predictions and the PIV experiments. From the comparison, it is shown that the IBM captures the mean and the secondary flow characteristic accurately for the square ribbed duct. The turbulence intensities predicted by the IBM agree well with the BFG prediction. Although, the IBM predicts somewhat faster decay of shear layer turbulence downstream of the rib region than the experimental data, the overall turbulent quantities match well between the IBM prediction and the experiments.

In Chapter 4, the CHT boundary condition of the IBM is validated by simulating a developing laminar flow on a two-dimensional flat plate at Re = 24,000. The interface wall temperature and the local Nusselt number along the plate are compared with the BFG prediction and the analytical result. It is shown that results from the IBM prediction and the BFG prediction

are almost identical. Furthermore, the difference between the IBM prediction and the analytical results are within 4% of each other.

In Chapter 5, the IBM with CHT boundary condition and fully developed assumption is validated by simulating a ribbed internal cooling passage at Re = 10,000. The heat transfer augmentation ratio (EF) of the IBM simulation is compared with the BFG prediction, LES-CHT simulation by Scholl *et al*. and the CHT experiment. Two different solid thermal properties (Case 1-accelerated and Case 2-physical) are used for the IBM simulation to compensate for the large time scale disparity between the convection in fluid and conduction in solid. It is notable that the mean heat transfer coefficient for both cases at statistically stationary conditions only differed by 1 percent. The comparison between the IBM and the BFG prediction show near identical results. Furthermore, the comparison with two other studies in the literature show that the results match reasonably well in all regions except at the rib front face. The comparison between the CHT and the iso-flux cases in all studies commonly show that the EF at the back face of the rib from the CHT case is lower than the EF from the iso-flux case by more than 40 %.

In conclusion, the comparison between the IBM prediction and other comparative studies shows that the IBM with the CHT boundary condition is comparable to other experimental as well as computations with BFG. Furthermore, it is found that using artificial solid thermal property can compensate for the characteristic time scale disparity between the fluid and the solid. Future work will focus on more intricate geometries representative of real turbine blade cooling arrangements.

Appendix A

In this chapter, the effect of the Biot number on the conjugate problem at steady state is further studied by simulating a laminar flow on a two-dimensional flat plate using the IBM framework. For this study, three different cases at similar Biot numbers with different Reynolds number, Prandtl number, and conductivity ratios are tested. Table A.1 shows conditions used for each case. The geometry used for this study can be found in Chapter 4.1.

Table A.1: Summary of Simulations at different condition

	Re	*Pr*	*K** (k_s/k_f)	Bi_{mean}
Case 1	10,000	4.15	9.7	0.219
Case 2	24,000	4.15	15	0.220
Case 3	24,000	10.09	20	0.227

Figure A.1 shows the interfacial temperature for three IBM cases and the analytical solution by Payvar. The temperature is non-dimensionalized as described in Chapter 4.2.1. Except the leading edge of the plate, where the large computational error is induced due to a thin developing boundary layer, the comparison among the three IBM predictions are within 5% of each other. Furthermore, the comparison between the IBM prediction and the analytical solution for all cases shows the error within 6 %.

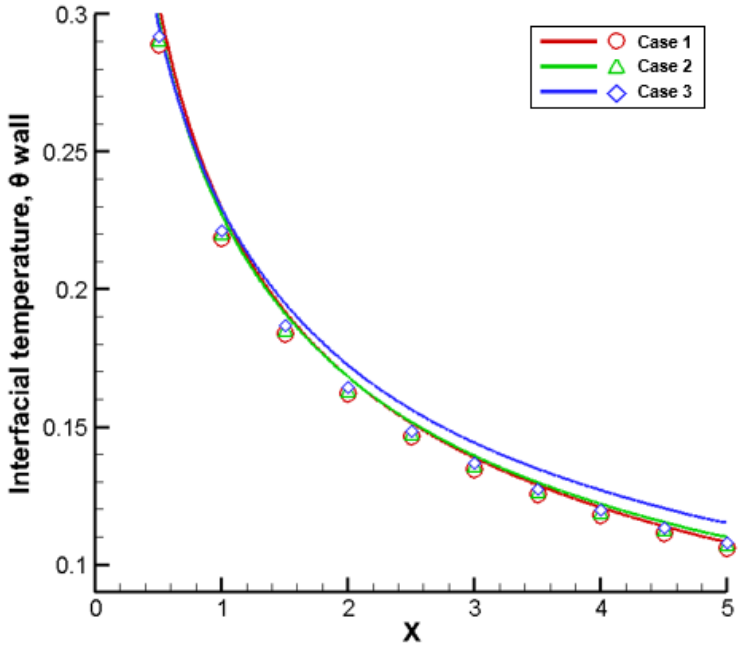

Figure A.1: Fluid-solid interface non-dimensional temperature along the streamwise direction. Symbols and solid lines represent analytical and IBM results, respectively.

Figure A.2 shows the local Nusselt number variation along the plate for the three IBM cases and the analytical solution by Payvar. The local Nusselt number is represented as the ratio of the conjugate case to the constant temperature case (see Chapter 4.2.2 for more detail). Except the leading edge of the plate, the local Nusselt numbers of all three cases are within 3 % of each other. Furthermore, the differences between the analytical solution and the IBM prediction are within 5% for all cases.

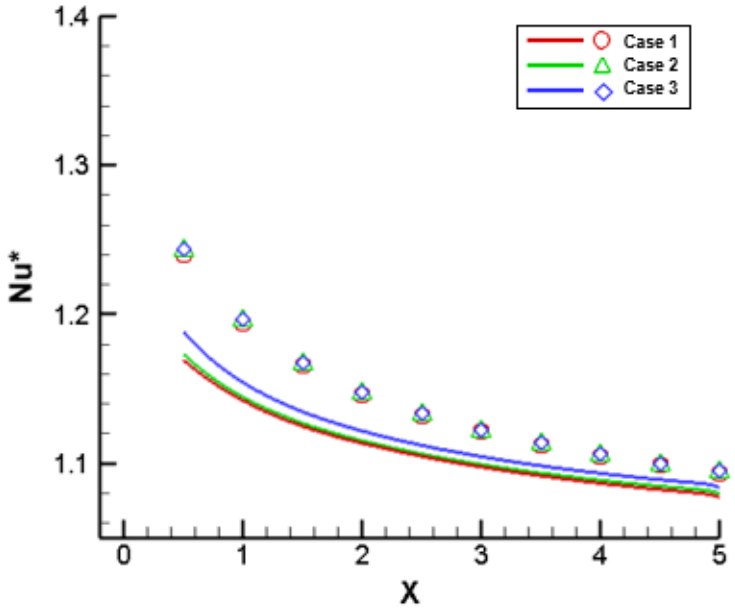

Figure A.2: Nu* variation along the streamwise direction. Symbols and solid lines represent analytical and IBM results, respectively.

From the comparison among three cases, it is found that even though Reynolds number, Prandtl number and the conductivity ratio are different, the temperature and the local Nusselt number at the fluid-solid interface are shown to be similar at thermal steady state when the Biot numbers are similar.

Appendix B

In this chapter, the local Nusselt number calculations of the IBM and the BFG using an accelerated property (Case 1) are further investigated. The time-averaged local Nusselt numbers of the IBM and the BFG cases are shown to be almost identical in Chapter 5.3.3. However, as can be seen in Figure B.1, the instantaneous fluctuation of the area-averaged heat transfer at the full CHT surface are different between the IBM and the BFG cases.

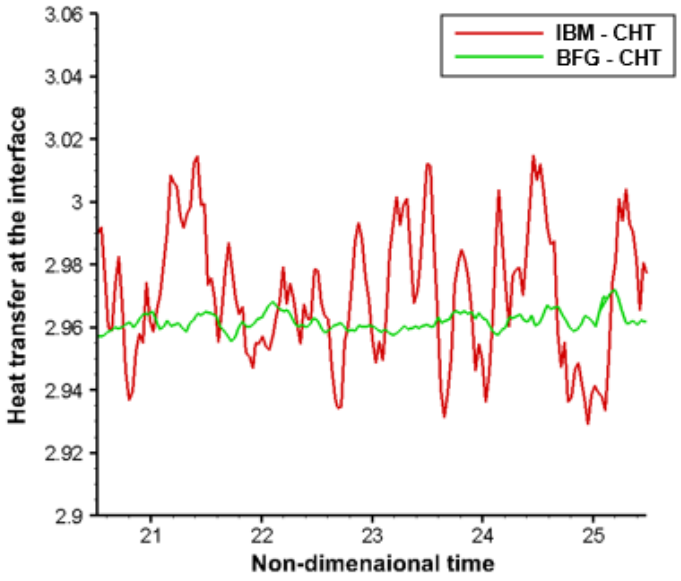

Figure B.1: Instantaneous heat transfer at the full CHT surface using accelerated property (Case 1).

The dissimilarity between the IBM and the BFG predictions can be surmised from the difference in calculating the local heat flux at the CHT surface. Figure B.2 and the equation B.1 show that the BFG calculates the heat flux based on the effective conductivity described in Chapter 2.5 and the temperature difference between the adjacent fluid and solid nodes.

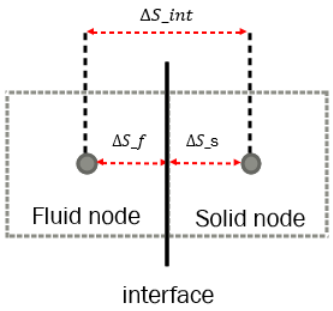

Figure B.2: Fluid and solid nodes involved in the heat flux calculation of BFG case.

$$q''_{BFG} = k_{eff} * \frac{T_{solid} - T_{fluid}}{\Delta S_{int}} \quad \text{(B. 1)}$$

However, Figure B.3 and the equation B.2 and show that the IBM uses the fluid conductivity and the temperature difference between the IB probe and the immersed surafce to calculate the heat flux.

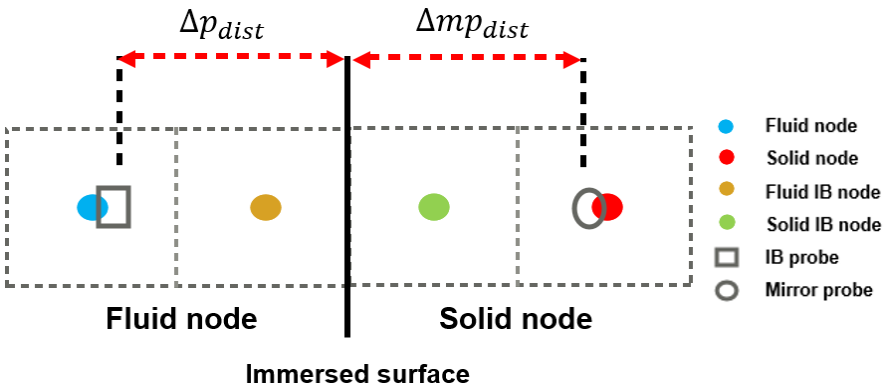

Figure B.3: Fluid and solid nodes involved in the heat flux calculation of IBM case.

$$q''_{IBM} = k_f * \frac{T_{immersed\ surface} - T_{IB\ probe}}{\Delta p_{dist}} \quad \text{(B. 2)}$$

Since the IB probe is located about one cell distance away from the fluid node, the temperature difference used in the heat flux calcualtion of the IBM fluctuates larger than what is used in the BFG over the time as shown in Figure B.4 and B.5. Accordingly, the area-averaged heat transfer at the full CHT surface of the IBM case also fluctuates in large amplitude over the time.

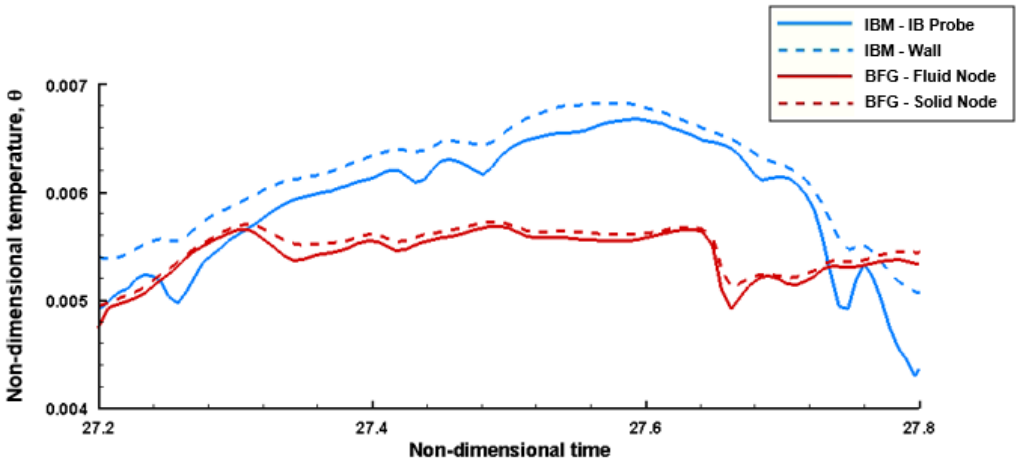

Figure B.4: Temperature fluctuation in time near the rib leading edge.

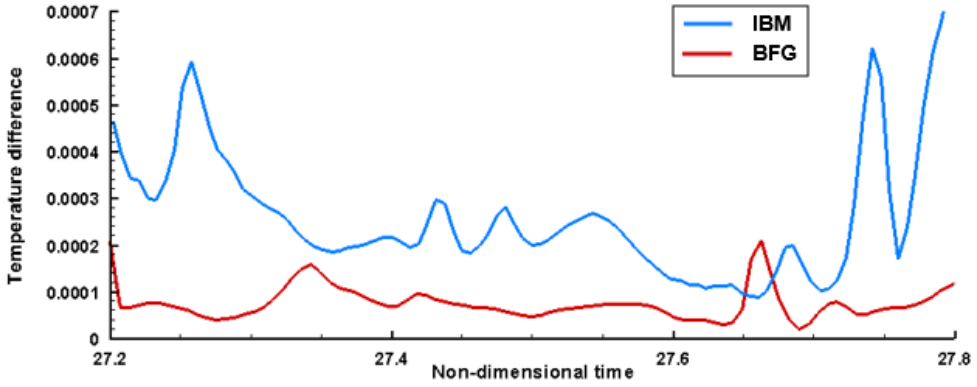

Figure B.5: Temperature difference fluctuation between the wall and fluid used in the heat flux calculation.

Even though the instantaneous fluctuation of the area-averaged heat transfer of the IBM and the BFG cases are different, the results are shown to be almost identical after sufficient amount of time averaging.

References

[1] B. Cukurel, “Conjugate Heat Transfer Investigation of a Fixed Rib Roughened Cooling Passage,” 2012.

[2] J.-C. Han, “Fundamental Gas Turbine Heat Transfer,” *J. Therm. Sci. Eng. Appl.*, vol. 5, no. 2, p. 021007, 2013.

[3] P. Ligrani, “Heat transfer augmentation technologies for internal cooling of turbine components of gas turbine engines,” *Int. J. Rotating Mach.*, 2013.

[4] E. Radenac, J. Gressier, and P. Millan, “Methodology of numerical coupling for transient conjugate heat transfer,” *Comput. Fluids*, vol. 100, pp. 95–107, 2014.

[5] V. Tom and R. Van den Braembussche, “A Novel Method for the Computation of Conjugate Heat Transfer With Coupled Solvers,” in *Int. Symp. on Heat Transfer in Gas Turbine Systems*, 2009.

[6] L. Casarsa and T. Arts, “Experimental Investigation of the Aerothermal Performance of a High Blockage Rib-Roughened Cooling Channel,” *J. Turbomach.*, vol. 127, no. 3, p. 580, 2005.

[7] L. Wang and B. Sundén, “Experimental investigation of local heat transfer in a square duct with various-shaped ribs,” *Heat Mass Transf.*, vol. 43, pp. 759–766, 2007.

[8] J. C. Han and J. S. Park, “Developing heat transfer in rectangular channels with rib turbulators,” *Int. J. Heat Mass Transf.*, vol. 31, no. 1, pp. 183–195, 1988.

[9] A. P. Rallabandi, N. Alkhamis, and J.-C. Han, “Heat Transfer and Pressure Drop Measurements for a Square Channel With 45 deg Round-Edged Ribs at High Reynolds Numbers,” *J. Turbomach.*, vol. 133, no. 3, p. 031019, 2011.

[10] Z. Ghorbani-Tari, L. Wang, and B. Sunden, “Effect of blockage-ratio on developing heat

transfer for a rectangular duct with transverse ribs," in *ASME Turbo Expo 2013*, 2013.

[11] A. Keshmiri, M. A. Cotton, and Y. Addad, "Numerical Simulations of Flow and Heat Transfer over Rib-Roughened Surfaces," in *17th Annual Conference of CFD Society of Canada, Ottawa*, 2009.

[12] A. Ooi, G. Iaccarino, P. A. Durbin, and M. Behnia, "Reynolds averaged simulation of flow and heat transfer in ribbed ducts," *Int. J. Heat Fluid Flow*, vol. 23, no. 6, pp. 750–757, 2002.

[13] C. Prakash and R. Zerkle, "Prediction of Turbulent Flow and Heat Transfer in a Ribbed Rectangular Duct With and Without Rotation," *J. Turbomach.*, vol. 117, no. April 1995, p. V03AT15A057, 1995.

[14] M. Ciofalo and M. W. Collins, "Large-Eddy Simulation of turbulent flow and heat transfer in plane and rib-roughened channels," *Int. J. Numer. Method Fluids*, vol. 15, no. February, pp. 453–489, 1992.

[15] D. K. Tafti, L. He, and K. Nagendra, "Large eddy simulation for predicting turbulent heat transfer in gas turbines," *Philos. Trans. R. Soc. A Math. Phys. Eng. Sci.*, vol. 372, no. 2022, pp. 20130322–20130322, 2014.

[16] O. Labbé, "Large-eddy-simulation of flow and heat transfer in a ribbed duct," *Comput. Fluids*, vol. 76, pp. 23–32, 2013.

[17] M. Lohász, P. Rambaud, and C. Benocci, "LES Simulation of Ribbed Square Duct Flow with FLUENT and Comparison with PIV Data," in *The 12th International Conference on Fluid Flow Technologies*, 2003.

[18] T. James and P. Tucker, "Large Eddy Simulation Of Turbine Internal Cooling Ducts," in *ASME 2013 International Mechanical Engineering Congress and Exposition*, 2013.

[19] A. V. Luikov, "Conjugate convective heat transfer problems," *Int. J. Heat Mass Transf.*,

vol. 17, no. 2, pp. 257–265, 1974.

[20] P. Payvar, “Convective heat transfer to laminar flow over a plate of finite thickness,” *Int. J. Heat Mass Transf.*, vol. 20, pp. 431–433, 1977.

[21] M. Mosaad, “Laminar forced convection conjugate heat transfer over a flat plate,” *Heat Mass Transf.*, vol. 35, no. 5, pp. 371–375, 1999.

[22] M. Lindstedt and R. Karvinen, “Conjugate heat transfer in a plate - One surface at constant temperature and the other cooled by forced or natural convection,” *Int. J. Heat Mass Transf.*, vol. 66, pp. 489–495, 2013.

[23] A. Lehtinen and R. Karvinen, “Analytical solution for a class of flat plate conjugate convective heat transfer problems,” *Front. Heat Mass Transf.*, vol. 2, no. 4, pp. 1–6, 2011.

[24] L. D. Hylton, M. S. Mihelc, E. R. Turner, D. A. Nealy, and R. E. York, “Analytical and Experimental Evaluation of the Heat Transfer Distribution Over the Surfaces of Turbine Vanes,” 1983.

[25] E. R. Turner, M. D. Wilson, L. D. Hylton, and R. M. Kaufman, “Turbine Vane External Heat Transfer,” 1985.

[26] P. C. Sweeney and J. F. Rhodes, “An Infrared Technique for Evaluating Turbine Airfoil Cooling Designs,” *J. Turbomach.*, vol. 122, no. 1, p. 170, 2000.

[27] E. Y. Jung, H. Chung, S. M. Choi, T.-K. Woo, and H. H. Cho, “Conjugate heat transfer on full-coverage film cooling with array jet impingements with various Biot numbers,” *Exp. Therm. Fluid Sci.*, vol. 83, pp. 1–8, 2017.

[28] W. Li, L. Yang, J. Ren, and H. Jiang, “Effect of thermal boundary conditions and thermal conductivity on conjugate heat transfer performance in pin fin arrays,” *Int. J. Heat Mass Transf.*, vol. 95, pp. 579–592, 2016.

[29] R. Fedrizzi and T. Arts, “Investigation of the Conjugate Convective-Conductive Thermal Behavior of a Rib-Roughened Internal Cooling Channel,” in *ASME Turbo Expo 2004*, 2004, pp. 45–53.

[30] F. Agostini and T. Arts, “Conjugate Heat Transfer Investigation of Rib-Roughened Cooling Channels,” in *Volume 3: Turbo Expo 2005, Parts A and B*, 2005, pp. 239–247.

[31] B. Cukurel and T. Arts, “Local Heat Transfer Dependency on Thermal Boundary Condition in Ribbed Cooling Channel Geometries,” in *ASME 2012 Summer Heat Transfer Conference*, 2013, vol. 135, no. 10.

[32] B. Cukurel, T. Arts, and C. Selcan, “Conjugate heat transfer characterization in cooling channels,” *J. Therm. Sci.*, vol. 21, no. 3, pp. 286–294, 2012.

[33] Z. Ke and J. Wang, “Conjugate heat transfer simulations of pulsed film cooling on an entire turbine vane,” *Appl. Therm. Eng.*, vol. 109, pp. 600–609, 2016.

[34] B. Facchini, A. Magi, and A. S. Del Greco, “Conjugate Heat Transfer Simultion Of A Radially Cooled Gas Turbine Vane,” in *ASME Turbo Expo 2004:Power for Land, Sea, and Air*, 2004, pp. 1–11.

[35] T. E. Dyson, D. G. Bogard, and S. D. Bradshaw, “Evaluation of CFD simulations of film cooling performance on a turbine vane including conjugate heat transfer effects,” *Int. J. Heat Fluid Flow*, vol. 50, pp. 279–286, 2014.

[36] R. P. Williams, T. E. Dyson, D. G. Bogard, and S. D. Bradshaw, “Sensitivity of the Overall Effectiveness to Film Cooling and Internal Cooling on a Turbine Vane Suction Side,” in *ASME Turbo Expo 2012*, 2012.

[37] T. I. Shih, X. Chi, K. M. Bryden, C. Alsup, and R. A. Dennis, “Effects of Biot Number on Temperature and Heat-Flux Distributions in a TBC-Coated Flat Plate Cooled by Rib-

Enhanced Internal Cooling by Rib-Enhanced Internal Cooling," in *ASME Turbo Expo 2009: Power for Land, Sea and Air*, 2009.

[38] Z. X. Han, B. H. Dennis, and G. S. Dulikravich, "Simultaneous prediction of external flow-field and temperature in internally cooled 3-D turbine blade material," *Int. J. Turbo Jet Engines*, vol. 18, no. 1, pp. 47–58, 2001.

[39] P. W. Giel, D. R. Thurman, G. J. Van Fossen, S. A. Hippensteele, and R. J. Boyle, "Endwall Heat Transfer Measurements in a Transonic Turbine Cascade," *J. Turbomach.*, vol. 120, no. 2, pp. 305–313, 1998.

[40] P. W. Giel, G. J. Van Fossen, R. J. Boyle, D. R. Thurman, and K. C. Civinskas, "Blade Heat Transfer Measurements and Predictions in a Transonic Turbine Cascade," *ASME 1999 Int. Gas Turbine Aeroengine Congr. Exhib.*, 1999.

[41] J. C. Song, J. Ahn, and J. S. Lee, "An immersed-boundary method for conjugate heat transfer analysis," *J. Mech. Sci. Technol.*, vol. 31, no. 5, pp. 2287–2294, 2017.

[42] D. Bohn, B. Bonhoff, H. Schönenborn, and H. Wilhelmi, "Validation of a Numerical Model for the Coupled Simulation of Fluid Flow and Diabatic Walls with Application to Film-cooled Turbine Blades," *VDI-Bericht*, vol. 1186, no. 6, pp. 272–295, 1995.

[43] D. E. Bohn, V. J. Becker, and A. U. Rungen, "Experimental and Numerical Conjugate Flow and Heat Transfer Investigation of a Shower-Head Cooled Turbine Guide Vane," in *ASME 1997 International Gas Turbine and Aeroengine Congress and Exhibition*, 1997.

[44] D. E. Bohn, V. J. Becker, K. A. Kusterer, Y. Otsuki, T. Sugimoto, and R. Tanaka, "3-D Internal Flow And Conjugate Calculations Of A Convective Cooled Turbine Blade With Serpentine-Shaped And Ribbed Channels," in *ASME 1999 International Gas Turbine and Aeroengine Congress and Exhibition*, 1999, vol. 3.

[45] D. E. Bohn and C. Tümmers, “Numerical 3-D Conjugate Flow and Heat Transfer Investigation Turbine Guide Vane With Reduced Cooling Fluid Mass Flow,” in *ASME Turbo Expo 2003: Proceedings of Power for Land, Sea, and Air*, 2003, pp. 1–8.

[46] D. Bohn, J. Ren, and K. Kusterer, “Systematic Investigation on Conjugate Heat Transfer Rates of Film Cooling Configurations,” *Int. J. Rotating Mach.*, vol. 3, pp. 211–220, 2005.

[47] N. Moritz, K. Kusterer, D. Bohn, T. Sugimoto, R. Tanaka, and T. Taniguchi, “Conjugate calculation of a film-cooled blade for improvement of the leading edge cooling configuration,” *Propuls. Power Res.*, vol. 2, no. 1, pp. 1–9, 2013.

[48] S. Scholl, T. Verstraete, F. Duchaine, and L. Gicquel, “Conjugate heat transfer of a rib-roughened internal turbine blade cooling channel using large eddy simulation,” *Int. J. Heat Fluid Flow*, vol. 61, pp. 650–664, 2016.

[49] D. K. Tafti, “Time-accurate techniques for turbulent heat transfer analysis in complex geometries,” *Adv. Comput. Fluid Dyn. Heat Transf. WIT Press*, vol. 41, pp. 217–264, 2010.

[50] J. Smagorinsky, “General circulation experiments with the primitive equations,” *Mon. Weather Rev.*, pp. 99–164, 1963.

[51] F. M. Najjar and D. K. Tafti, “Study of discrete test filters and finite difference approximations for the dynamic subgrid-scale stress model,” *Phys. Fluids*, vol. 8, no. 4, pp. 1076–1088, 1996.

[52] M. Germano, U. Piomelli, P. Moin, and W. H. Cabot, “A dynamic subgrid-scale eddy viscosity model,” *Phys. Fluids A*, vol. 3, no. 7, pp. 1760–1765, 1991.

[53] and S. L. P.Moin, K.Squires, W.Cabot, “A dynamic subgrid-scale model for compressible turbulence and scalar transport,” *Phys. Fluids A*, vol. 3, no. 1–2, pp. 3–12, 1991.

[54] S. V. Patankar, C. H. Liu, and E. M. Sparrow, “Fully Developed Flow and Heat Transfer in

Ducts Having Streamwise-Periodic Variations of Cross-Sectional Area," *J. Heat Transfer*, vol. 99, no. 2, p. 180, 1977.

[55] L. W. Zhang, D. K. Tafti, F. M. Najjar, and S. Balachandar, "Computations of flow and heat transfer in parallel-plate fin heat exchangers on the CM-5: Effects of flow unsteadiness and three-dimensionality," *Int. J. Heat Mass Transf.*, vol. 40, no. 6, pp. 1325–1341, 1997.

[56] A. Gilmanov and F. Sotiropoulos, "A hybrid Cartesian/immersed boundary method for simulating flows with 3D, geometrically complex, moving bodies," *J. Comput. Phys.*, vol. 207, no. 2, pp. 457–492, 2005.

[57] K. Nagendra, D. K. Tafti, and K. Viswanath, "A new approach for conjugate heat transfer problems using immersed boundary method for curvilinear grid based solvers," *J. Comput. Phys.*, vol. 267, pp. 225–246, 2014.

[58] A. Allievi and R. Bermejo, "A generalized particle search-locate algorithm for arbitrary grids," *J. Comput. Phys.*, vol. 132, no. 2, pp. 157–166, 1997.

[59] G. V. Diurno, E. Balaras, and U. Piomelli, "Wall-layer models for LES of separated flows," in *Modern simulation strategies for turbulent flows*, B. Geurts, Ed. 2001, pp. 207–222.

[60] D. R. Chapman, "Computatisnal Aerodynamics Development and Outlook," *AIAA J.*, vol. 17, no. 12, pp. 1293–1313, 1979.

[61] S. Patil and D. Tafti, "Large-Eddy Simulation With Zonal Near Wall Treatment of Flow and Heat Transfer in a Ribbed Duct for the Internal Cooling of Turbine Blades," *J. Turbomach.*, vol. 135, no. 3, p. 031006, 2013.

[62] W. Cabot and P. Moin, "Approximate Wall Boundary Conditions in the Large-Eddy Simulation of High Reynolds Number Flow," *Flow, Turbul. Combust.*, vol. 63, no. 1, pp. 269–291, 1999.

[63] W. M. Kays, “Turbulent Pratidtl Number - Where Are We?,” *Max Jakob Meml. Award Lect.*, pp. 1–12, 1992.

[64] L. Casarsa and T. Arts, “Aerodynamic performance investigation of a Rib Roughened Cooling Channel Flow with high blockage ratio.,” in *11th International Symposium on Applications of Laser Techniques to Fluid Mechanics, Lisbon, Portugal*, 2002, no. 1.

[65] L. Casarsa, “Aerodynamic performance investigation of a fixed rib-roughened internal cooling passage,” 2003.

[66] B. Cukurel, C. Selcan, and T. Arts, “Film Cooling Extraction Effects on the Aero-Thermal Characteristics of Rib Roughened Cooling Channel Flow,” *J. Turbomach.*, vol. 135, no. 2, 2012.

[67] S. Scholl, T. Verstraete, J. Torres-Garcia, F. Duchaine, and L. Gicquel, “Influence of the thermal boundary conditions on the heat transfer of a rib-roughened cooling channel using les,” *Proc. Inst. Mech. Eng. Part A J. Power Energy*, vol. 229, no. 5, pp. 498–507, 2015.

[68] D. K. Tafti, “Evaluating the role of subgrid stress modeling in a ribbed duct for the internal cooling of turbine blades,” *Int. J. Heat Fluid Flow*, vol. 26, no. 1, pp. 92–104, 2005.

[69] W. York, “A Robust Conjugate Heat Transfer Methodology with Novel Turbulence Modeling Applied to Internally-Cooled Gas Turbine Airfoils,” Clemson University, 2006.

[70] L. He and M. L. G. Oldfield, “Unsteady Conjugate Heat Transfer Modeling,” *J. Turbomach.*, vol. 133, no. 3, p. 031022, 2011.

[71] He, L., and Tafti, D., “Evaluating the immersed boundary method in a ribbed duct for the internal cooling of turbine blades,” In *ASME Turbo Expo 2015: Turbine Technical Conference and Exposition, American Society of Mechanical Engineers, Montreal, Quebec, Canada*, 2015.